JGR Biogeosciences

RESEARCH ARTICLE
10.1029/2018JG005002

Key Points:
- Warm springs usually enhance springtime forest GPP and evapotranspiration but result in water limitation that reduces late-season fluxes
- A photosynthesis model with plant stress parameterized by measured leaf water potential can track interannual GPP and SIF variations well
- SIF_{yield} shows dampened variations compared to LUE, which explains the smaller observed reduction in SIF than GPP during drought period

Supporting Information:
- Supporting Information S1

Correspondence to:
L. He and C. Frankenberg,
cfranken@caltech.edu;
lhe@caltech.edu

Citation:
He, L., Wood, J. D., Sun, Y., Magney, T., Dutta, D., Köhler, P., et al. (2020). Tracking seasonal and interannual variability in photosynthetic downregulation in response to water stress at a temperate deciduous forest. *Journal of Geophysical Research: Biogeosciences*, *125*, e2018JG005002. https://doi.org/10.1029/2018JG005002

Received 30 DEC 2018
Accepted 13 JUL 2020
Accepted article online 28 JUL 2020

Tracking Seasonal and Interannual Variability in Photosynthetic Downregulation in Response to Water Stress at a Temperate Deciduous Forest

Liyin He[1], Jeffrey D. Wood[2], Ying Sun[3], Troy Magney[1,4], Debsunder Dutta[1,5], Philipp Köhler[1], Yongguang Zhang[6], Yi Yin[1], and Christian Frankenberg[1,7]

[1]Division of Geological and Planetary Sciences, California Institute of Technology, Pasadena, CA, USA, [2]School of Natural Resources, University of Missouri, Columbia, MO, USA, [3]School of Integrative Plant Sciences, Section of Soil and Crop Science, Cornell University, Ithaca, NY, USA, [4]Department of Plant Sciences, University of California, Davis, CA, USA, [5]Department of Civil Engineering, Indian Institute of Science, Bangalore, India, [6]Jiangsu Provincial Key Laboratory of Geographic Information Science and Technology, International Institute for Earth System Sciences, Nanjing University, Nanjing, China, [7]Jet Propulsion Laboratory, California Institute of Technology, Pasadena, CA, USA

Abstract The understanding and modeling of photosynthetic dynamics affected by climate variability can be highly uncertain. In this paper, we examined a well-characterized eddy covariance site in a drought-prone temperate deciduous broadleaf forest combining tower measurements and satellite observations. We find that an increase in spring temperature usually leads to enhanced spring gross primary production (GPP), but a GPP reduction in late growing season due to water limitation. We evaluated how well a coupled fluorescence-photosynthesis model (SCOPE) and satellite data sets track the interannual and seasonal variations of tower GPP from 2007 to 2016. In SCOPE, a simple stress factor scaling of Vcmax as a linear function of observed predawn leaf water potential (ψ_{pd}) shows a good agreement between modeled and measured interannual variations in both GPP and solar-induced chlorophyll fluorescence (SIF) from the Global Ozone Monitoring Experiment-2 (GOME-2). The modeled and satellite-observed changes in SIF_{yield} are ~30% smaller than corresponding changes in light use efficiency (LUE) under severe stress, for which a common linear SIF to GPP scaling would underestimate the stress reduction in GPP. Overall, GOME-2 SIF tracks interannual tower GPP variations better than satellite vegetations indices (VIs) representing canopy "greenness." However, it is still challenging to attribute observed SIF variations unequivocally to greenness or physiological changes due to large GOME-2 footprint. Higher-resolution SIF data sets (e.g., TROPOMI) already show the potential to well capture the downregulation of late-season GPP and could pave the way to better disentangle canopy structural and physiological changes in the future.

1. Introduction

Accurate estimates of gross primary production (GPP) are important for tracking the response of plants to environmental stress and have important applications for crop and forest management (Beer et al., 2010). In recent decades, growing-season length and peak vegetation growth have increased due to the global climate change and human activities, which have a potential positive impact on terrestrial carbon uptake (Buitenwerf et al., 2015; Chen et al., 2019; Huang et al., 2018; Park et al., 2019; Zhu et al., 2016). However, late growing-season photosynthesis is highly uncertain and sensitive to climate (Buermann et al., 2018; Wolf et al., 2016; Zhang et al., 2020). In a warming climate, water availability plays an increasingly important role as a limiting factor for late growing-season terrestrial photosynthesis (Lian et al., 2020; Zhang et al., 2020). Therefore, it is crucial to evaluate the impact of water availability on photosynthesis, and how well observations and photosynthesis models can track late growing-season photosynthesis, with a particular focus on responses to water stress.

Satellite observations have been widely used to monitor vegetation growth status and estimate GPP at global scales (Schimel et al., 2015). Traditional reflectance-based vegetation indices (VIs) such as the Normalized Difference Vegetation Index (NDVI) (Tucker, 1979) and Enhanced Vegetation Index (EVI) (Huete et al., 2002) are appropriate for tracking canopy "greenness" but are sometimes insensitive to environmental stress on diurnal and/or short time scales (e.g., heat waves and water stress) (Dobrowski et al., 2005; Rossini et al., 2015). At longer time scales, changes in pigment composition associated with environmental stress can

be detected from space, such as the carotenoid:chlorophyll index (CCI, Gamon et al., 2016), but it is unclear how responsive this signal is to rapid changes in photosynthesis. A potential solution to track dynamic and reversible adaptation of plants to stress is to monitor changes in the chlorophyll *a* fluorescence yield, which typically decreases following a rapid increase in nonphotochemical quenching (NPQ) and reduction in photosynthetic efficiency.

To model GPP from greenness indices, the light use efficiency (LUE)-based model (Monteith, 1972) with remote sensing observations of absorbed light has been developed to derive GPP (Running et al., 2004):

$$GPP = PAR \times fPAR \times LUE = APAR \times LUE, \quad (1)$$

where *PAR* is incident photosynthetically active radiation; *fPAR* is the fraction of PAR absorbed by plants (usually inferred by VIs), and *LUE* is the efficiency of the plant's conversion of absorbed radiation to CO_2 uptake—which responds dynamically to changes in temperature, water stress, and/or the light environment. Calculating LUE mostly relies on simple scaling functions based on air temperature and vapor pressure deficit (VPD) (Myneni et al., 2015; Running et al., 2004; Turner et al., 2006; Yuan et al., 2007), which is associated with large uncertainties.

Another strategy to relate remote sensing measurements to photosynthetic efficiencies arises from the light reactions of photosynthesis. There are three primary dissipation pathways for the energy absorbed by chlorophyll molecules in the antenna system (Porcar-Castell et al., 2014): photochemical quenching (PQ), fluorescence, and heat dissipation.

At scales relevant to satellite remote sensing, the emission of steady-state fluorescence illumination is referred to as solar-induced chlorophyll fluorescence (SIF), the emission of red and near-infrared light in the 650 to 850 nm spectral range. Recent global satellite products of SIF from the Greenhouse Gases Observing Satellite (GOSAT) (Frankenberg et al., 2011; Guanter et al., 2012; Joiner et al., 2011), Global Ozone Monitoring Experiment-2 (GOME-2) (Joiner et al., 2013; Köhler et al., 2015), SCanning Imaging Absorption spectroMeter for Atmospheric CHartographY (SCIAMACHY) (Köhler et al., 2015), Orbiting Carbon Observatory-2 (OCO-2) (Frankenberg et al., 2014; Sun et al., 2017, 2018), Chinese global carbon dioxide monitoring satellite (TanSat) (Liu et al., 2018), and TROPOspheric Monitoring Instrument (TROPOMI) (Guanter et al., 2015; Köhler et al., 2018) have shown promise to constrain large-scale carbon fluxes from space (Li, Xiao & He, 2018; MacBean et al., 2018; Song et al., 2018; Sun et al., 2015, 2017; Zhang et al., 2016).

Analogous to the LUE model for GPP, SIF emission from the canopy can be described according to

$$SIF = PAR \times fPAR \times \Phi_F \times \Omega = APAR \times SIF_{\text{yield}}, \quad (2)$$

where Φ_F is the actual fluorescence yield, defined as the emitted fluorescence per unit of radiation absorbed, neglecting potential reabsorption of far-red light within the canopy; Ω is the probability of fluorescence photons escaping the canopy; SIF_{yield} is the effective fluorescence yield (Guanter et al., 2014) and is computed as the product of actual fluorescence yield and escape probability.

Since SIF is emanating from the light reaction centers during photosynthesis, it is expected to be related to the electron transport rate, and thus a proxy of photosynthesis (Gu et al., 2019; Perez-Priego et al., 2015). Recent studies show robust empirical linear scaling between GPP and SIF for different vegetation types at the canopy scale (Frankenberg et al., 2011; Guanter et al., 2014; Guan et al., 2016; He et al., 2020; Li, Xiao, He, Altaf Arain et al., 2018; Magney et al., 2019; Smith et al., 2018; Song et al., 2018; Sun et al., 2018; Verma et al., 2017; Wood et al., 2017; Zhang et al., 2016). The primary reason for such strong relationships is that APAR acts as a common variable in both equations, driving GPP and SIF. The second-order effect is that the SIF_{yield} correlates with LUE at the canopy scale in most cases (Magney et al., 2019; Yang et al., 2015). This indicates that SIF not only contains information on light interception but also physiological responses to environmental stress, which are reflected in changes in photosynthetic yields. Therefore, SIF is expected to correlate better with GPP than VIs. However, the SIF_{yield}-*LUE* relationship is complex, causing deviations from a simple linear scaling and is only empirically represented in models (van der Tol et al., 2014). Positive relationships between SIF_{yield} and *LUE* have been reported at the canopy scale across different ecosystems

(Porcar-Castell et al., 2014; van der Tol et al., 2014; Yang et al., 2015), but there is limited understanding of the covariation of the SIF_{yield} and *LUE* under different environmental conditions.

The potential of satellite SIF to track drought has been reported in some recent papers. For example, Sun et al. (2015) explored the potential of GOME-2 SIF to monitor the drought spatial and temporal dynamics; Verma et al. (2017) showed that the relationship between OCO-2 SIF and GPP is robust at canopy scale under different environmental conditions in grasslands; Yoshida et al. (2015) found that SIF_{yield} and *fPAR* both decline during the drought, and GPP losses in mixed forest is mainly due to LUE reduction, while GPP losses in croplands and grasslands are mostly driven by changes in *fPAR*. However, few studies have focused on evaluating the performance of photosynthesis models and long-term satellite SIF and VI observations to track flux tower GPP during the late growing season, when vegetation is exposed to varying stress intensities. Also, it remains unclear how the SIF_{yield}-*LUE* relationship responds to different levels of water stress in forest ecosystem.

Here, we address this knowledge gap by using long-term observations at the Missouri Ozark AmeriFlux site (US-MOz), a drought-prone, temperate deciduous forest site located in central Missouri, to examine the relationships among eddy covariance GPP, satellite SIF, and VIs, as well as LUE-based satellite GPP products and a detailed coupled photosynthesis and SIF modeling exercise. The study site regularly experiences seasonal drought in later summer, allowing us to investigate the complex relationship between SIF_{yield} and *GPP* under varying degrees of stress. The US-MOz site also provides a unique set of predawn leaf water potential (ψ_{pd}) measurements, which enable us to link efficiency changes directly to plant water status. Our main questions are as follows: (1) What are the drivers of interannual variations (IAV) in late growing-season GPP and are these related to systematic changes in the seasonal cycle? (2) How well does a biophysical process-based model track the IAV in both flux tower GPP and measured SIF? (3) How well can SIF track the seasonal and IAV of GPP compared with MODIS VIs and the MODIS GPP product?

2. Materials and Methods

2.1. Field Site and Measurements

The AmeriFlux site US-MOz (38.744°N, 92.200°W) is a second growth upland oak-hickory forest, located in the transitional zone between the central hardwood and central grassland regions in the United States (Gu et al., 2015; Gu, Pallardy, Yang, et al., 2016; Wood et al., 2018). The dominant tree species at the site are white oak (*Quercus alba* L.), black oak (*Q. velutina* Lam.), shagbark hickory (*Carya ovata* (Mill.) K. Koch), sugar maple (*Acer saccharum* Marsh.), and eastern redcedar (*Juniperus virginiana* L.). The site lies in a warm, humid, and continental climate zone, with an average annual temperature of about 13°C, and average annual precipitation around 1,140 mm. Physiological water stress is common during the growing season (Gu et al., 2015) and is tightly controlled by within-season precipitation variability (Gu, Pallardy, Hosman, et al., 2016), because plant available water in the comparatively shallow soils can be quickly depleted. Water stress is therefore a strong regulator of ecosystem carbon and water fluxes (Gu, Pallardy, Yang, et al., 2016; Wood et al., 2018; Yang et al., 2010), the partitioning of available energy into sensible and latent heat (Gu et al., 2006), and is related to tree mortality (Gu et al., 2015; Wood et al., 2018).

In this study, we used half-hourly net ecosystem exchange (NEE), GPP, and evapotranspiration (ET) derived from continuous eddy covariance measurements from 2007 to 2016. The reader is referred to Gu et al. (2012) and Gu, Pallardy, Yang, et al. (2016) for a more complete description of the instrumentation on the 32 m walk-up tower used to observe ecosystem fluxes and the eddy covariance flux calculations. Briefly, the moving point threshold test developed by Gu et al. (2005) was used to objectively estimate friction velocity thresholds for screening nighttime NEE data for periods of low turbulence. Data gaps were filled using the mean diurnal variation approach (Gu, Pallardy, Yang, et al., 2016). GPP was estimated by subtracting daytime observations of NEE from soil respiration measured using flow through non-steady state chambers (Yang et al., 2010), noting that soil respiration is often the largest component of ecosystem respiration (Hermle et al., 2010; Li et al., 2012; Tang et al., 2008). We also point out that there are uncertainties and potential biases with any partitioning method (Wohlfahrt & Lianhong, 2015), and indeed, recent evidence points to potentially large biases in the common NEE partitioning methods (Keenan et al., 2019; Wehr et al., 2016).

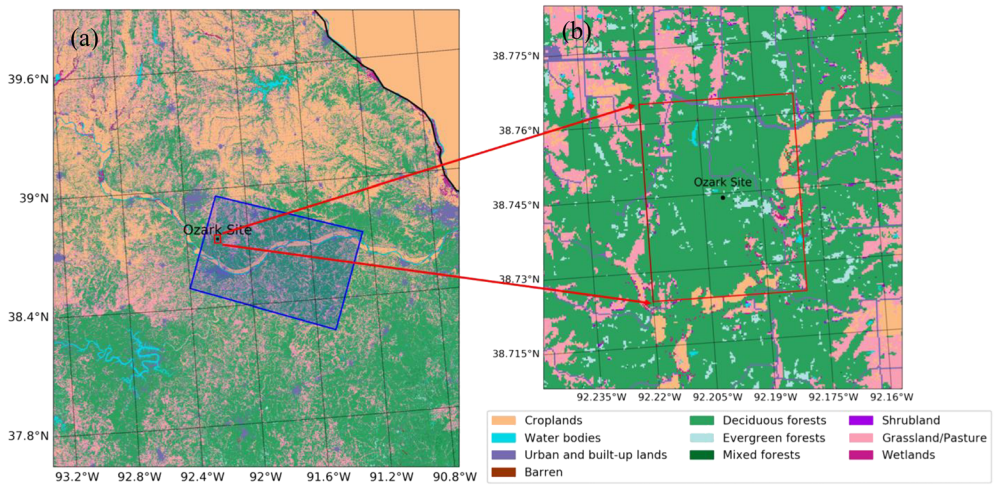

Figure 1. An example of a GOME-2 footprint relative to MODIS aggregation used in the analysis: (a) The transparent light blue polygon represents a GOME-2 footprint from an overpass on 16 June 2013. All GOME-2 footprints with the distance between central longitude/latitude and US-MOz less than 0.75° are used in the analysis. Red boundaries indicate the 0.02° fine-resolution of MODIS products aggregated in this study. (b) The enlarged map shows the location of the flux tower and surrounding land cover. The 30-m cropland data layer (CDL) by U.S. Department of Agriculture (USDA) in 2016 is used for land cover classification.

We also used records of incident PAR, air temperature (Ta), VPD, precipitation, volumetric soil water content (SWC) at 10 cm depth, and ψ_{pd}. Predawn leaf water potential is measured before sunrise and is a useful indicator of plant and ecosystem physiological water stress, as it reflects the root zone soil water potential and the degree to which leaves are able to rehydrate overnight (Gu et al., 2015; Gu, Pallardy, Hosman, & Sun, 2016; Wood et al., 2018). At weekly to stem abundance before dawn and ψ_{pd} was determined using the pressure chamber technique (Pallardy et al., 2018, 1991). An overview of the long-term GPP, Ta, and precipitation can be found in Figure S1 in the supporting information.

2.2. Satellite Data Sets

2.2.1. GOME-2 SIF

We used GOME-2 SIF (~80 km × 40 km footprint before July 2013, ~ 40 km × 40 km after) at 740 nm retrieved using a statistical approach (Köhler et al., 2015) and applied a daily correction factor to convert the instantaneous SIF signal to a daily average SIF. GOME-2 SIF soundings with center longitudes/latitudes within 0.75° from the US-MOz were extracted from 2007 to 2016. Figure 1a shows an example of extracted footprint on 16 June 2013 in the direct vicinity of the tower. SIF observations were filtered by removing soundings with cloud fractions larger than 20% and then aggregated to monthly averages.

2.2.2. MODIS NDVI, EVI, NIRv, fPAR, and GPP

We derived commonly used VIs (including NDVI, EVI, and near infrared reflectance of terrestrial vegetation [NIRv]) from the MODIS MCD43A4 v006 using the following formulas (Badgley et al., 2017; Didan et al., 2015; Huete et al., 1997; Liu & Huete, 1995):

$$NDVI = \frac{NIR - R}{NIR + R}, \tag{3}$$

$$EVI = G \times \frac{NIR - R}{NIR + C_1 \times R - C_2 \times B + L}, \tag{4}$$

$$NIRv = NIR \times NDVI, \tag{5}$$

where NIR, R, and B stand for the spectral reflectance acquired in the near-infrared, red, and blue bands, respectively; G is a scaling factor; C_1 and C_2 are constants to account for atmospheric scattering; and L is the coefficient of canopy background adjustment. For MODIS EVI derivation, G, C_1, C_2, and L are set to 2.5, 6, 7.5, and 1, respectively. MCD43A4 provides daily "nadir" 500 m pixel size reflectance data corrected

by using a bidirectional reflectance distribution function model, which minimizes the bias in reflectance measurements introduced by different illumination and observation geometries. The MODIS MCD15A3H fPAR product, a 4-day composite data set with 500 m spatial resolution, was also used in this study to estimate the relative contribution of fPAR to the GPP-SIF relationship. We also included the MODIS MYD17A2H V006 8-day GPP product with 500 m spatial resolution in the analysis to evaluate its performance compared to flux tower GPP and SIF. MODIS products were aggregated at 0.02° within the flux tower in the study, which contain a large proportion of homogeneous forests (Figure 1b).

2.2.3. GOSIF Data Set

To reconcile the large footprint of GOME-2 SIF, we also used the machine-learning generated GOSIF data set at 0.05° spatial resolution, aggregated at monthly averages from 2007 to 2016. GOSIF is trained using OCO-2 SIF and colocated MODIS MCD43C4 (Collection 6, 0.05°) BRDF-corrected EVI, and meteorology variables (including PAR, VPD, and Ta) obtained from the NASA reanalysis MERRA-2 data set (Li & Xiao, 2019).

2.2.4. TROPOMI SIF

To explore the potential of new satellite SIF at higher spatiotemporal resolution in the drought monitoring, we also evaluated the performance of TROPOMI SIF, with ~7 km × 3.5 km spatial resolution and near-global daily coverage (Köhler et al., 2018). The TROPOMI instrument onboard the European Sentinel-5 Precursor satellite was launched on 13 October 2017. As for GOME-2, the daily correction factor was also applied to TROPOMI SIF to convert instantaneous SIF to a daily average. In this study, we aggregated TROPOMI SIF monthly at 0.05° in 2018 to investigate its seasonal variation at US-MOz.

2.2.5. Spatial Aggregation of the Remote Sensing Data

In the fine-scale analysis, we tried to make the raw satellite data (at native resolution) comparable to the flux tower GPP. Therefore, we used the GOME-2 SIF footprints with the central longitude/latitude 0.75° nearby the flux tower, as well as MODIS data 0.02° within the flux tower. Note that the footprints of GOME-2 are quite large and composed of different landcovers other than forests, such as croplands and grasslands. This makes it hard to fairly compare the GOME-2 SIF and MODIS products. To deal with this problem, we also conducted an analysis gridding both GOME-2 and MODIS products at 0.25° and then examined these two at the same spatial aggregation.

2.3. GPP and SIF Simulations

The Soil Canopy Observation, Photochemistry, and Energy fluxes (SCOPE) model is a 1-D integrated radiative transfer and energy balance model, which simulates photosynthesis, fluorescence, the surface energy balance, and reflectance/emission spectra (Van Der Tol et al., 2009). Within SCOPE, empirical models of the rate coefficients of NPQ and SIF_{yield} are used, which are based on leaf level experiments (van der Tol et al., 2014), and parameterized as a function of the photosynthetic PSII yield (ΦP) computed by the Farquhar, von Caemmerer, Berry (FvCB) model (Farquhar et al., 1980). SCOPE provides two different parameterizations of the leaf-level SIF_{yield} (ΦF)-ΦP relationship. The first (SCOPE 1) is derived from measurements of leaves of various species experiencing progressive drought (Flexas et al., 2002), and the second (SCOPE 2) is derived from cotton leaves with less exposure to stress (van der Tol et al., 2014). The parameterizations diverge toward lower photosynthetic yields (i.e., at high light and generally more stressed conditions) (Magney et al., 2017; van der Tol et al., 2014). We used half-hourly meteorological variables measured at the US-MOz from 2007 to 2016 for the SCOPE simulations. The important meteorological drivers include incoming shortwave and longwave radiation, air temperature, atmospheric pressure, actual vapor pressure, and wind speed. Leaf area index (LAI) measured at the site and typical values of leaf biochemical parameters (e.g., Vcmax25 = 80 μ mol m^{-2} s^{-1} and Chl content = 100 μ g/cm^2) are used for the simulations. The key biochemical parameter Vcmax is scaled by a stress factor (SF) [0–1], which is a common way of implementing soil moisture stress in land surface models (Oleson et al., 2013). Further, the model also incorporates detailed calculation of temperature dependence of the photosynthetic biochemical parameters (Dutta et al., 2019). The rationale for using SCOPE simulations is to (1) model GPP and SIF changes at the canopy level with proper parameterization of Vcmax; (2) compare the measured SIF_{yield}-LUE at the canopy level with expectations from the SCOPE parameterization ΦF-ΦP at the leaf level, with an emphasis on the fractional change of each term under stress (LUE, SIF_{yield}, ΦF, and ΦP).

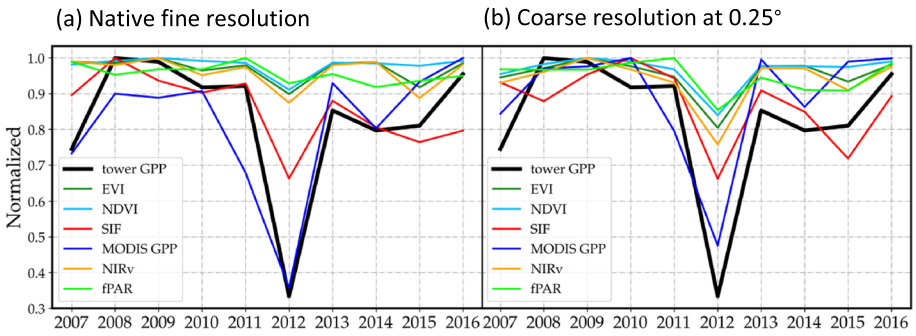

Figure 2. Average flux tower GPP, MODIS EVI, NDVI, and NIRv and GOME-2 SIF during JJA from 2007 to 2016. (a) MODIS products are aggregated at 0.02°, and native GOME-2 SIF footprints of the central longitude and latitude within 0.75° from the flux tower are used. (b) MODIS products and GOME-2 SIF are aggregated at 0.25°. All variables are scaled by the corresponding maximum value. RMSE and R^2 between flux tower GPP and SIF, NDVI, EVI, NIRv, fPAR, MODIS GPP, NDVI*PAR, EVI*PAR, NIRv*PAR, and fPAR *PAR are reported in Table S1. Raw data of flux tower GPP, SIF, MODIS GPP, NDVI, EVI, NIRv, and fPAR are reported in Table S2.

2.4. Singular Value Decomposition Analysis

To extract the coherent patterns contributing to the seasonal and IAV of GPP, we perform a singular value decomposition (SVD) analysis to obtain the principal components (PCs) that explain the time series of eddy covariance GPP. We assemble monthly flux tower GPP from 2007 to 2016 into matrix A with m rows and n columns, where $m = 10$ is the number of years and $n = 12$ is the number of months. Using SVD, we factorize A into three matrices $A = USV^{\mathrm{T}}$, where the columns of U (m by m) and V (n by n) are left and right singular vectors and S (m by n) is a diagonal matrix with nonnegative real numbers in descending order. The matrix A with both seasonal and interannual information can then be reconstructed by

$$A = \sum_{i=1}^{m} u_i \times s_i \times v_i^T, \tag{6}$$

where u_i is the ith singular vector with length m, containing temporal loadings for individual year; v_i is the ith singular vector with length n, containing the ith principal component (PCi, equivalent to seasonal dynamics of GPP); and s_i is the singular value of ith component. In other words, monthly GPP of each year can be reconstructed as the linear combination of PCs weighted by the corresponding temporal loadings. In our study, we found that the first three PCs are sufficient to explain most of the variance (around 90%).

3. Results

3.1. Long-Term Analysis of Flux Tower Observations and Satellite Remote Sensing

3.1.1. IAV of GPP, NDVI, EVI, NIRv, fPAR, and SIF

To evaluate the performance of MODIS VIs, MODIS GPP, and GOME-2 SIF in tracking IAV of flux tower GPP during JJA, we normalized each variable by its maximum value (Figure 2). At both fine and coarse aggregations, MODIS GPP and GOME-2 SIF capture the magnitude of the IAV of flux tower GPP better than NDVI, EVI, and NIRv. In 2012 U.S. Drought (Boyer et al., 2013; Hoerling et al., 2014; Karl et al., 2012; Mallya et al., 2013; Parazoo et al., 2015; Sun et al., 2015), flux tower GPP decreased by nearly 70% compared to 2008, the most productive year. Meanwhile, MODIS GPP decreased by around 55% and SIF dropped by around 33%, whereas only a 10% decline of VIs and fPAR was observed at the fine scale 0.02° aggregation (Figure 2a). Little fluctuation in VIs and fPAR in JJA from 2007 to 2016 indicates that this ecosystem maintains a relatively stable canopy structure during the peak growing season, which is supported by measurement of LAI in the field (Figure S2). Therefore, a substantial part of the summer interannual GPP variations can be attributed to changes in LUE, which are better reflected in MODIS GPP and GOME-2 SIF observations.

We also recognize a larger decrease of VIs and fPAR found at the coarser aggregation at 0.25° (Figure 2b) in 2012, implying that the structure of nonforest ecosystems in the vicinity (crops and grasslands) might be influenced more strongly than forest ecosystems during the drought. This confounding factor makes it

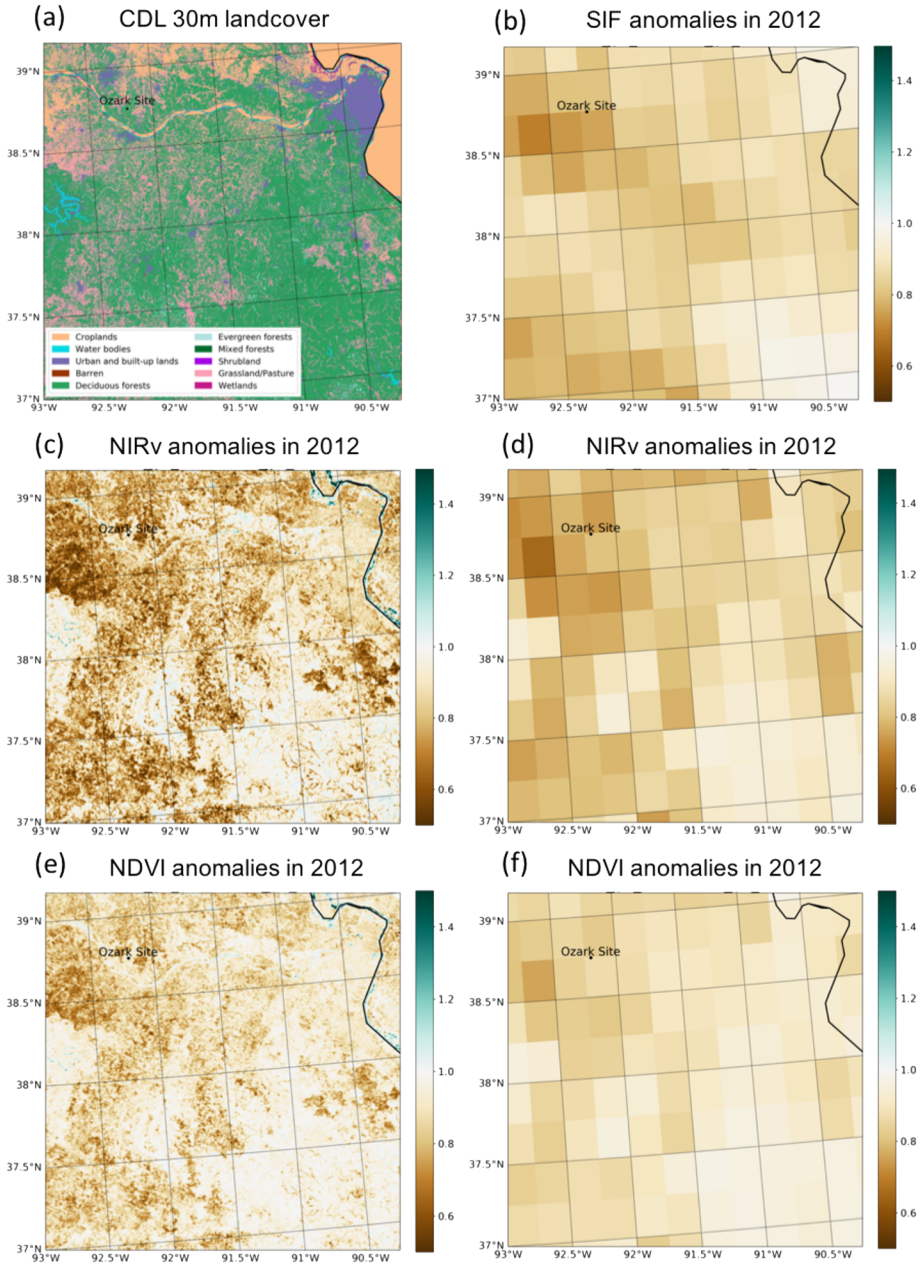

Figure 3. (a) The landcover map based on the USDA CDL data set in 2016. The spatial distributions of NIRv and NDVI anomalies at native fine resolution (500 m) are shown in (c) and (e). The spatial distributions of SIF, NIRv, and NDVI anomalies at coarse resolution (0.25°) are shown in (b), (d), and (f).

difficult to evaluate whether the stronger reduction in observed SIF is supporting the claim that SIF reacts more strongly to dynamic environmental stress or whether the large GOME-2 pixels just include more information from crops and grasslands, which reacted more strongly. Therefore, we studied the spatial pattern of the anomalies of GOME-2 SIF, MODIS NDVI, and NIRv at 0.25° to in 2012 drought from the normal years. The fractional anomaly at each grid was computed as

$$X_{\text{anomaly}} = \frac{X_{JJA_{2012}}}{X_{JJA_{\text{mean}}}},$$

where X represents the variable (such as SIF, NIRv, and NDVI). $X_{JJA_{2012}}$ is the average of X during JJA in 2012, while $X_{JJA_{\text{mean}}}$ is the multiyear average of X during JJA from 2007 to 2016.

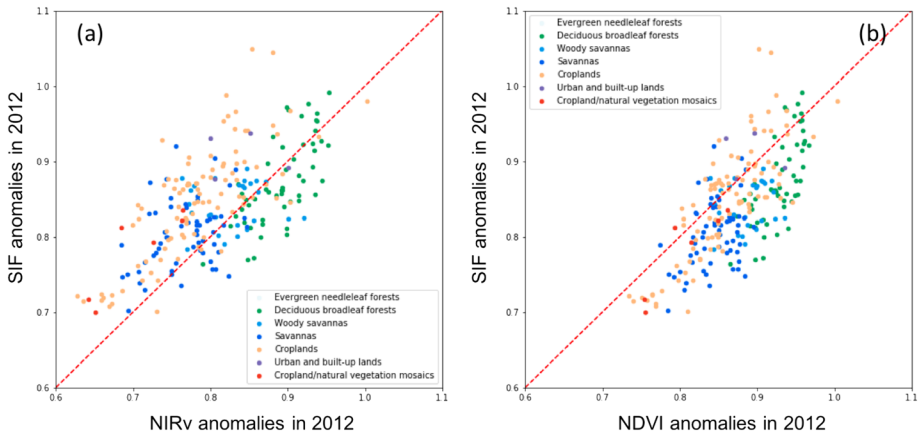

Figure 4. The anomalies of (a) SIF-NIRv and (b) SIF-NDVI during 2012 drought. Different colors represent different land types.

This analysis was necessary to (1) examine whether the spatial pattern of SIF and NDVI/NIRv anomalies is consistent using the data set aggregated at the same resolution and (2) explore SIF–NDVI/NIRv relation across different types of biomes during the drought.

The CDL 30-m landcover map around Ozark is shown in Figure 3a. Figures 3c and 3e show the spatial pattern of $NIRv_{anomaly}$ and $NDVI_{anomaly}$ at native fine resolution (500 m), whereas Figures 3b, 3d, and 3f are based on coarse resolution (0.25°). At the fine resolution, only a few areas actually show enhancements, mostly aligned along rivers. In general, we find a larger reduction of NIRv compared to NDVI in most regions. At the coarse resolution (0.25°), around 30% reduction was observed for SIF and NIRv at the Ozark grid cell, while only a 10% reduction was found for NDVI, which could be due to NDVI saturation effects.

We also quantified the relationship of $SIF_{anomaly}$-$NIRv_{anomaly}$ and $SIF_{anomaly}$-$NDVI_{anomaly}$ corresponding to different land covers using all the data in the state of Missouri gridded at 0.25° (Figure 4). In general, the spatial patterns in the IAV of all remotely sensed data sets are tightly correlated. However, we find that the relationship also depends on the land cover, with more fractional reduction observed for SIF than NIRv and NDVI in forests during the 2012 drought, which corroborates that some of the stress-related reduction in GPP over forests is captured by SIF. This analysis underscores the importance of considering the spatial heterogeneity in the complex natural ecosystem when interpreting remote sensing data.

3.1.2. Seasonal Variations of GPP, NDVI, EVI, NIRv, fPAR, and SIF

Figures 5a, 5c, and 5e show the seasonal variations at the fine spatial scale, with MODIS products aggregated at 0.02°, and GOME-2 SIF of the central longitude and latitude within 0.75° from the flux tower. Figures 5b, 5d, and 5f show the seasonal variations with MODIS products and GOME-2 SIF gridded at 0.25°. All variables are normalized based on min-max scaling from [0, 1]. For both spatial aggregations, NDVI and fPAR do not track the GPP seasonality during the mid-to-late growing season (i.e., July, August, and September). Flux tower GPP decreases by 50% from July to September; however, NDVI and fPAR remain almost constant. To evaluate whether this discrepancy can be caused by changes in available light, we used PAR measured at the flux tower to scale the VIs to estimate APAR, which was calculated as fPAR*PAR (Figures 5e and 5f). We found a closer agreement between NIRv*PAR and EVI*PAR with flux tower GPP seasonality. This indicates that, in general, the seasonal cycle of GPP at the US-MOz site is mostly dominated by changes in absorbed light and not photosynthetic efficiencies and, thus, the accurate estimate of absorbed light is important to obtain the accurate GPP estimate at the seasonal scale. Using NDVI, the relationship is weaker, with a pronounced broadening in the seasonal cycle compared to GPP. The MODIS fPAR algorithm is similar to NDVI, only considering the reflectance at red and near infrared bands (Myneni et al., 2015), thus showing strong similarity to NDVI. Other VIs, such as the EVI, reduce the saturation problem and the effects of atmospheric interferences and soil background brightness (Huete et al., 2002). In addition, NIRv contains the information of the pixel reflectance attributed to vegetation and mitigates the mixed-pixel problem

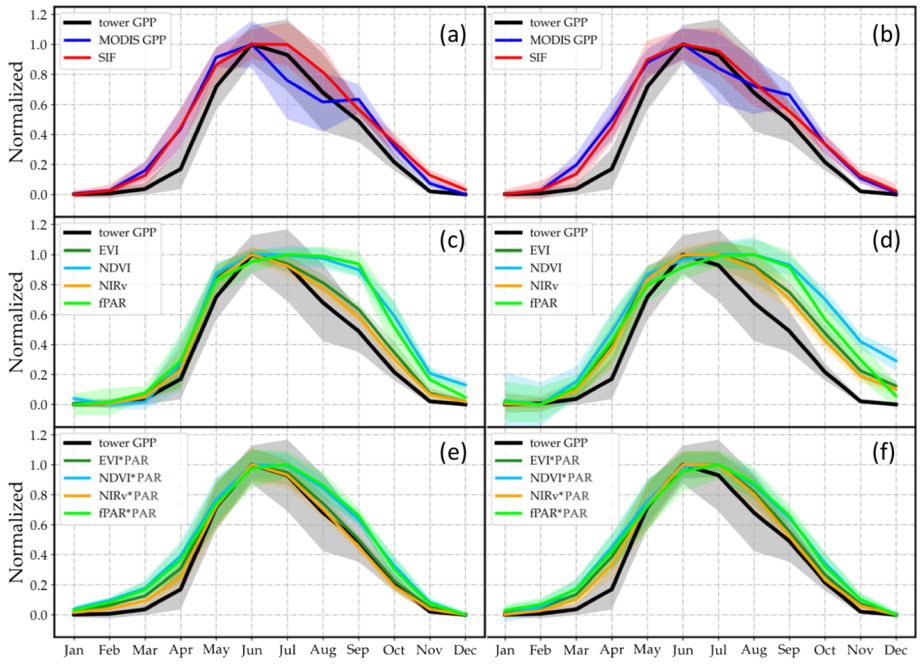

Figure 5. Seasonal cycles of monthly mean flux tower GPP, MODIS GPP, GOME-2 SIF, MODIS EVI, NDVI, NIRv and fPAR, EVI*PAR, NDVI*PAR, NIRv*PAR, and fPAR*PAR with the shadow regions representing ±1 standard deviation from 2007 to 2016. In (a), (c), and (e), MODIS products are aggregated at 0.02°, and native GOME-2 SIF footprints of the central longitude and latitude within 0.75° from the flux tower are used. In (b), (d), and (f), MODIS products and GOME-2 SIF are gridded at 0.25°. All variables are linearly normalized based on min-max scaling to fall in [0, 1]. RMSE and R^2 between flux tower GPP and SIF, NDVI, EVI, NIRv, fPAR, MODIS GPP, NDVI*PAR, EVI*PAR, NIRv*PAR, and fPAR *PAR are reported in Table S3.

(Badgley et al., 2017). Here, NIRv and EVI perform best at the seasonal scale, while SIF increases earlier than reflectance-based VIs at the onset of growing season. An explanation for this could be that GOME-2 observations are obtained with large footprints that are influenced by the mixed forest and crops or grasslands in the vicinity of the flux tower.

Interestingly, MODIS GPP appears to closely follow GOME-2 SIF in the early part of the season but deviates from a typical seasonality in July and August, with persistent reductions in GPP. This is mainly related to the LUE parameterization in the MODIS model, which appears to strongly overestimate the sensitivity to VPD or temperature. In fact, the LUE parameterization in MODIS GPP appears to worsen the agreement compared to the raw VIs multiplied by PAR.

3.1.3. Diurnal Variations of LUE

Diurnal LUE changes may introduce bias when we intend to estimate daily average SIF (and GPP) using an instantaneous SIF signal. Here we evaluate the potential bias in the daily GPP estimate using the LUE at GOME-2 and OCO-2 overpass times. The average diurnal cycle of LUE in the summer period (DOY 150–240) from 2007 to 2016 is shown in Figure 6a. Here, the apparent LUE is approximated by GPP/PAR, with the assumption that fPAR is almost constant within the growing season and not changing within a day, which is supported by fPAR measurements in the field. LUE is higher in the morning and late afternoon and lower around solar noon. A diurnal hysteresis in LUE was observed, with higher LUE in the morning than afternoon for the same Earth-Sun geometry. This is usually caused by increases in temperature and VPD during the day, causing an LUE asymmetry in the diurnal cycle. This temporal variation of LUE may cause a bias for upscaling instantaneous GPP (GPP_{inst}) to daily GPP (GPP_{daily}), which depends on the time chosen to infer daily GPP. In a similar fashion, there may be similar biases when scaling instantaneous satellite SIF observations to daily averages. This analysis gives insights into interpreting SIF observations at different times of satellite overpasses, as well as quantifying bias of temporal scaling of SIF from snapshots taken at a certain time of a day to an estimate of daily average.

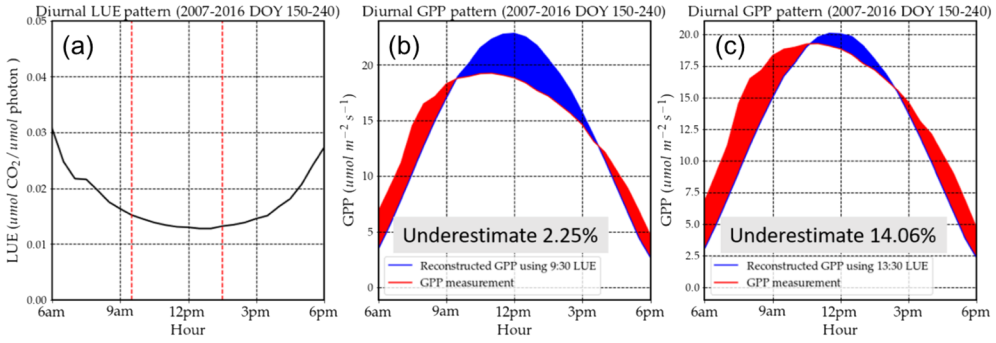

Figure 6. (a) Average diurnal GPP/PAR pattern during JJA including both sunny and cloudy observations from 2007 to 2016. The red dashed lines represent different GOME-2 and OCO-2 overpasses, ~ 9:30 and 13:30 at local time, respectively. In (b) and (c), the diurnal patterns of GPP from measurements and the LUE upscaling approach are represented by the red and blues lines, respectively. Blue and red shaded regions represent overestimation by upscaled and measured GPP, respectively.

Then, we evaluated the reconstructed diurnal GPP pattern based on the LUE at 9:30 and 13:30 local time, the overpass times of GOME-2 and OCO-2, respectively. The reconstruction was performed by multiplying the instantaneous LUE by an average diurnal PAR pattern in the summer period including both sunny and cloudy observations. The reconstructed GPP and flux tower GPP measurements in summer using different instantaneous LUE are shown in Figures 6b and 6c. There was no significant bias in upscaling GPP based on LUE at 9:30 because the instantaneous value was a good estimator of the daily average. However, daily GPP was largely underestimated when using LUE at 13:30, since the instantaneous value was almost at the minimum daily value. Therefore, based on the seasonal averaged diurnal shape of GPP at this site, we expect less bias in the GOME-2 daily normalized SIF compared to OCO-2 under the assumption that (i) the SIF_{yield} is correlated with LUE and (ii) instantaneous SIF is scaled to daily SIF using the Earth-Sun geometry. However, we have to consider that the variability of SIF_{yield} is dampened compared to LUE, which might reduce this bias at midday.

3.2. Impact of Spring Temperature on Annual GPP

Here, we investigated the control of late growing-season GPP at the US-MOz site. Specifically, we aim to isolate specific variations of GPP seasonality that might be related to the interannual variability of GPP. The SVD analysis of eddy covariance GPP provides us with a pattern of three leading PCs scaled by corresponding singular values, that is, computed as $s_1 \times v_1^T$, $s_2 \times v_2^T$, and $s_3 \times v_3^T$ in Figures 7a–7c. The first three PCs explain 90% of the seasonal variability across 10 years. As expected, the shape of $s_1 \times v_1^T$ reflects the mean seasonal GPP cycle, while the following PCs reflect deviations from the mean. $s_2 \times v_2^T$ increases rapidly in early spring and remains positive until summer, representing a "trade-off" between spring gain and summer loss. $s_3 \times v_3^T$ follows a "W" pattern (see Figure 7c) and can be interpreted as a widening or narrowing of the overall growth period. Total GPP (the integration of GPP over 12 months) of the three PCs is 124.0, 4.0, and −3.2, respectively, and denoted as r_1, r_2, r_3. Total annual GPP can thus be approximated by the sum of $u_1 r_1$, $u_2 r_2$, and $u_3 r_3$. Since r_1 is significantly larger than r_2 and r_3, annual total GPP is mainly controlled by u_1.

A strong negative correlation is observed for u_1 and u_2 (Figure 7d). Meanwhile, u_2 is strongly correlated with annual spring temperature (Figure 7e), even if the more extreme drought years of 2007 and 2012 are excluded. This indicates that in years with higher spring temperature, $s_2 \times v_2^T$ captures the seasonal change with an increase in spring GPP but a decrease in the summer. As this feature correlates negatively with u_1, there is an overall decrease in annual GPP during all years with an early spring.

We found that spring GPP, SIF, and NEE are strongly driven by spring temperature (Figures 8a and 8b). Larger spring GPP, SIF, and more net ecosystem CO_2 uptake (i.e., more negative NEE) are observed for years with warmer spring (Figures 8c and 8d). However, warmer springs do not guarantee an increase in annual GPP and net ecosystem CO_2 uptake (e.g., in 2007 and 2012), which is due to higher ET during the onset of the growing season or low precipitation throughout the growing season. In addition, higher spring temperature

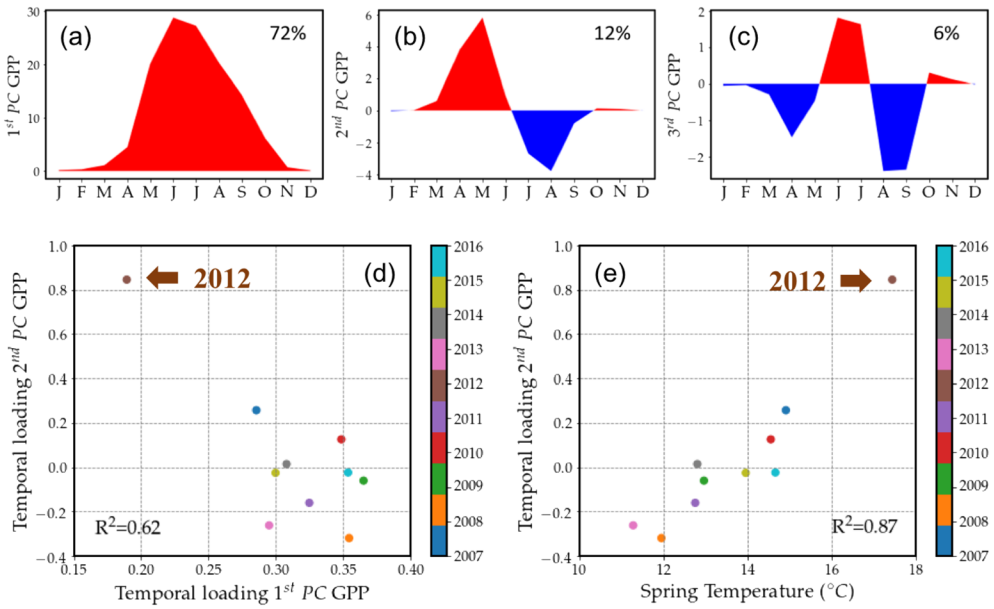

Figure 7. Three leading PCs scaled by corresponding singular value $s_1 \times v_1^T$, $s_2 \times v_2^T$, and $s_3 \times v_3^T$ are shown in (a)–(c), explaining 72%, 12%, and 6% of variability in monthly GPP. Negative correlation between temporal loading u_1 and u_2 is shown in (d), and positive correlation between average spring temperature and temporal loading u_2 is shown in (e), with different color representing different years.

is consistently associated with lower net ecosystem CO_2 uptake and GPP in the summer (Figures 8e and 8f), which might attributed to less photosynthetic efficiency due to water limitation as well as more active respiratory processes at higher temperature and will be discussed in section 4.1.

To investigate whether the other parameters follow similar PCs in the SVD decomposition, we performed the same SVD analysis for flux tower ET measurements, satellite VIs, and SIF (Figure 9). The analysis including tower measurements and satellite observations consistently shows that the second PC is similar to the one for GPP, especially for SIF and ET. Since ET is linked with stomatal conductance and water use efficiency, it is expected to covary with GPP, explaining strong correlations among all the three PCs of ET and GPP. For remote sensing data, SIF performs most similar to the tower GPP in higher orders, with three leading PCs explaining 78%, 8%, and 5% of variability, and all shapes having high similarity to the PCs for GPP. In contrast, NDVI is largely dominated by the first PC, which explains 92% variability, and only 4% and 2% variability can be explained by the second and third PC. This implies that SIF is more sensitive in capturing the signal of stress-induced GPP "seasonal-shifted" dynamics than VIs and thereby helps better estimate the interannual GPP change patterns.

3.3. SCOPE Modeled GPP and SIF Track Flux Tower GPP

To better understand the underlying mechanisms, we simulate the IAV of GPP and SIF using the SCOPE model and evaluate how well SCOPE captures flux tower GPP variations with proper parameterization. During drought, plants may experience a combination of both canopy structural changes and physiological stress, imposed by atmospheric conditions such as elevated temperature and VPD but also through soil moisture deficits. Usually, the structural change is reflected in VIs; however, capturing physiological changes is challenging. Disentangling these two effects is important to determine the information SIF can provide for quantifying physiological stress beyond canopy structural changes. In this section, we show the effects of incorporating physiological stress on both primary production and fluorescence with SCOPE simulations. In SCOPE, environmental stress affects photosynthesis and fluorescence purely through changes in humidity and temperature, as a soil moisture model is missing. As in many models, the drought stress through soil moisture variations is incorporated through a SF [0, 1] to scale the maximum carboxylation rate (Vcmax at 25°C) effectively reducing photosynthesis and thus also stomatal conductance, which is equivalent to the soil water stress parameter (BTRAN) in the Community Land Model (Oleson et al., 2013).

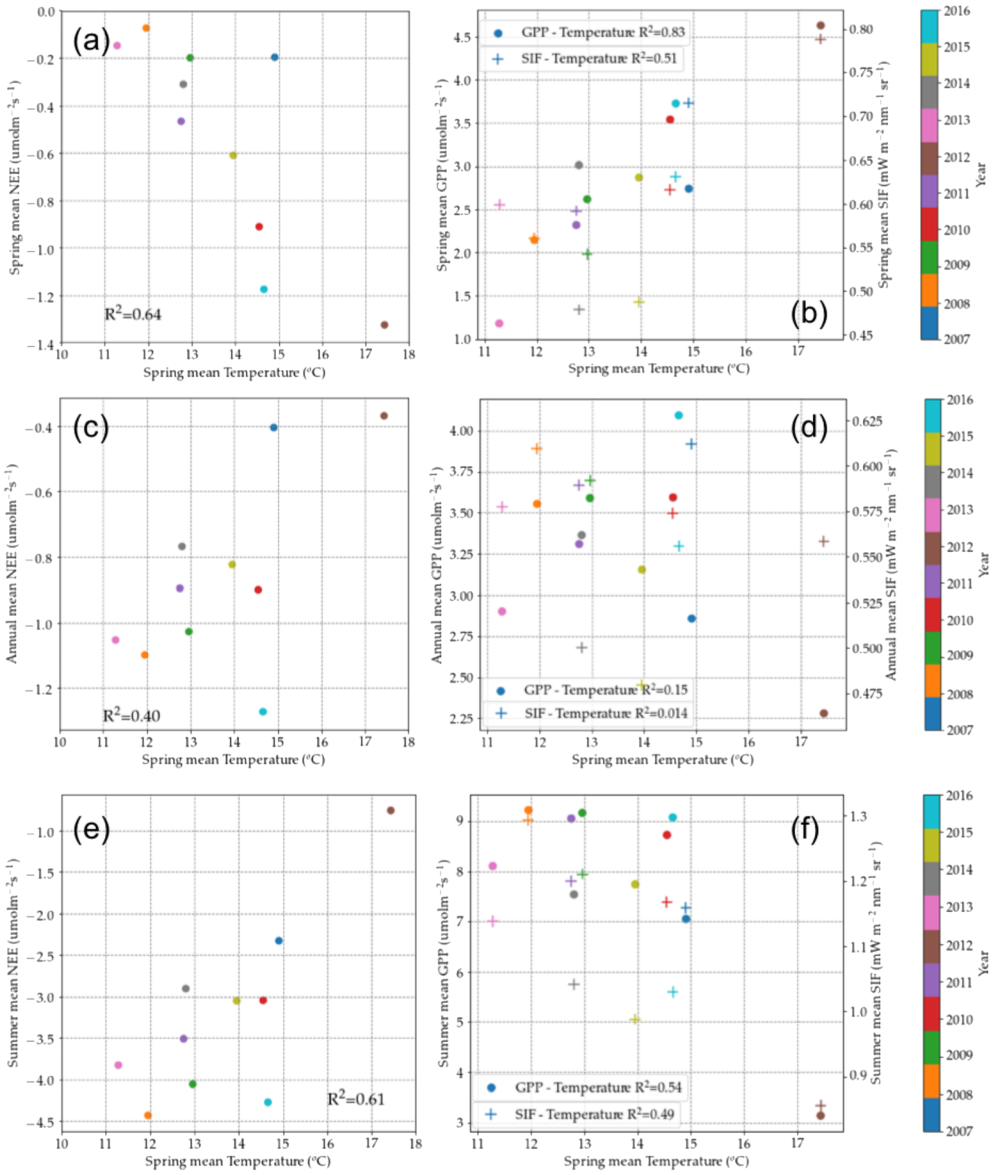

Figure 8. The relationship between spring temperature with spring mean NEE, GPP, and SIF (a and b); annual mean NEE, GPP, and SIF (c and d); and summer NEE, GPP, and SIF (e and f). Different colors represent different years. Spring months are defined as March, April, and May.

We performed two simulations: (1) without any soil moisture stress (SF = 1) and (2) with variable SF as a time series computed as a function of predawn leaf water potential ψ_{pd} (Figure 10a). We found that the ratio of observed flux tower GPP to the GPP modeled using SCOPE (Case 1), $\frac{towerGPP}{GPPmodeledwithnoSF}$, is correlated with ψ_{pd} (Figure 10a), and proportional to the stress experienced by the plant. The SF is calculated from this relationship based on the first-order linear regression of $\frac{towerGPP}{GPPmodeledwithnoSF}$ and ψ_{pd}, which is used for the simulations of Case 2. In both cases, we used LAI and meteorological data (including air temperature, VPD, radiation, and wind speed) collected at the flux tower to drive the model. Thus, a basic interannual variation of stress due to changing atmospheric conditions is already included in Simulation 1.

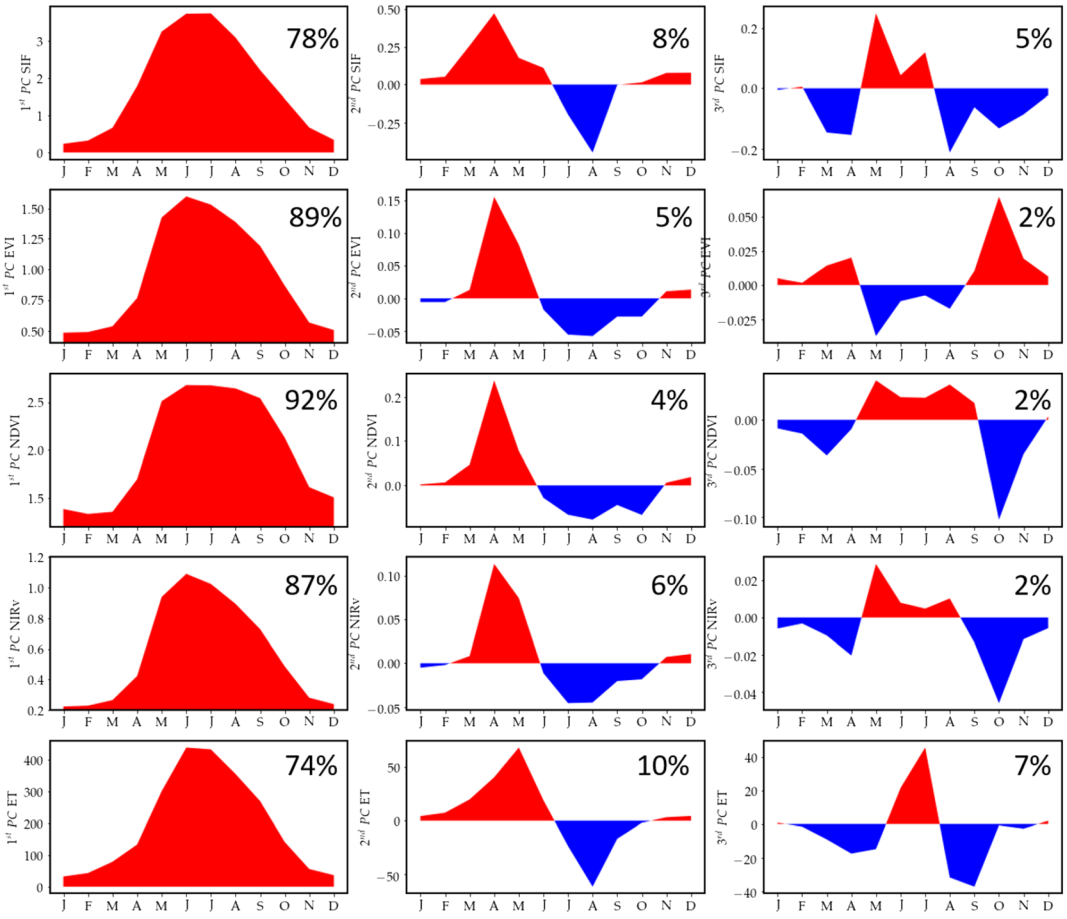

Figure 9. Three leading PCs of SIF, EVI, NDVI, NIRv, and ET (top to bottom rows, respectively) scaled by corresponding singular value $s_1 \times v_1^T$, $s_2 \times v_2^T$, and $s_3 \times v_3^T$, with the fraction of explained variance shown for each.

The first case (green line in Figure 10b), with no soil moisture-driven physiological stress, can be interpreted as the GPP of plants around Ozark, only considering atmospheric variations across different years. The second case (red line in Figure 10b), with SF, indicates the effect of soil moisture availability on GPP. In the 2012 drought, higher air temperature and larger VPD only account for a 20% reduction in GPP. However, we found an additional 35% reduction in GPP upon introduction of SF in the model, leading to a 55% total reduction in GPP, close to the 65% reduction in GPP observations, underlining that our ad hoc SF parameterization worked well. Overall, comparing the two cases (with and without the SF) using the SCOPE model

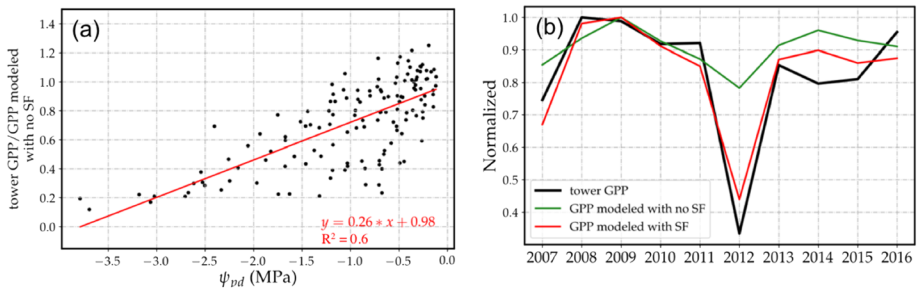

Figure 10. (a) The ratio of flux tower GPP (biweekly average) to GPP modeled by SCOPE (biweekly average) with no scaling factor (SF) introduced as the function of ψ_{pd} (MPa). (b) Average of flux tower GPP, GPP modeled by SCOPE with/without SF during JJA from 2007 to 2016. All variables are scaled by the corresponding maximum value.

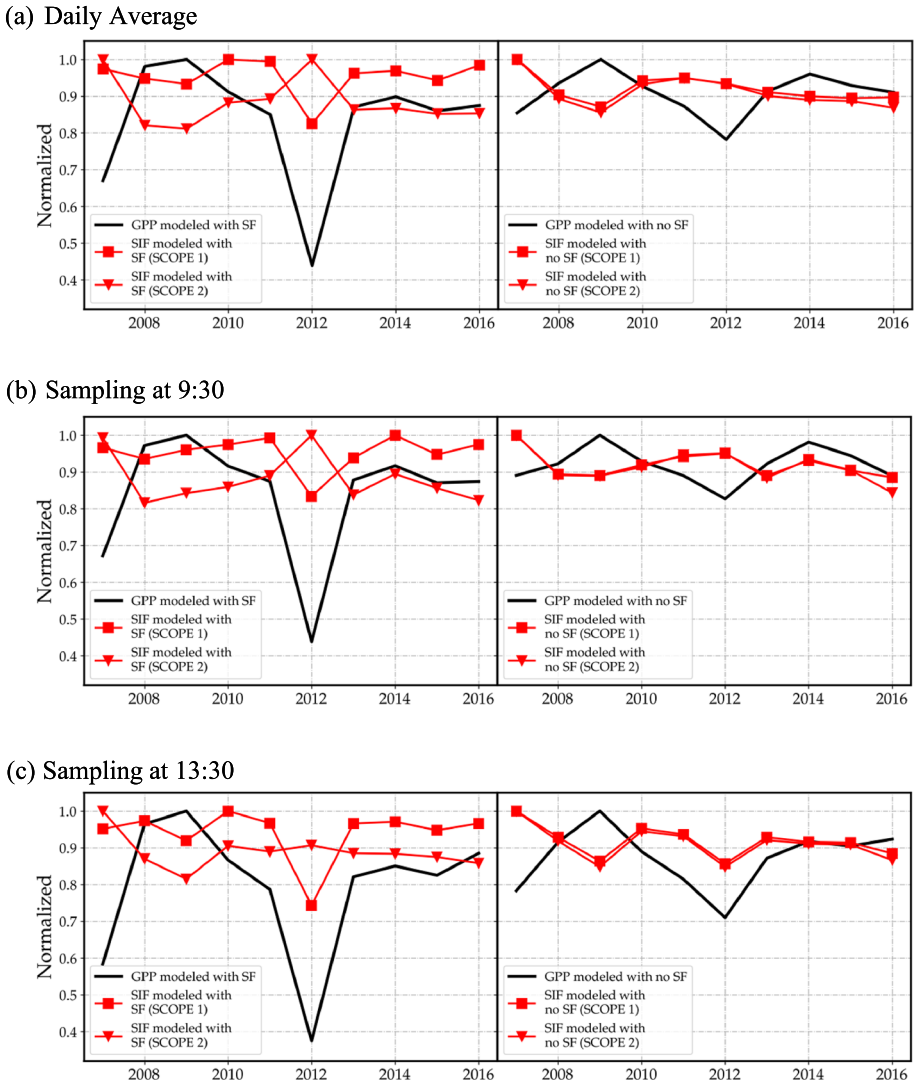

Figure 11. Average of GPP, SIF modeled by SCOPE with/without SF using two different parameterizations of *ΦF* versus *ΦP* during JJA from 2007 to 2016. All variables are scaled by the corresponding maximum value. Note that SCOPE 1 refers to empirical leaf-level *ΦF-ΦP* relationship based on various leaf samples experienced progressive drought (Flexas et al., 2002) and SCOPE 2 refers to *ΦF-ΦP* relationship experimented on healthy cotton leaves (van der Tol et al., 2014).

provides a good way to decouple canopy structural changes and physiological stress on GPP. The latter was found to contribute more in the 2012 drought, which underscores the importance of a physiology related signal to monitor terrestrial GPP changes using remote sensing.

To evaluate how SIF might change within a modeling framework, we look into the IAV of modeled SIF (with and without SF introduced) at three different timescales (daily average, 9:30 and 13:30) and compare its magnitude against the corresponding IAV of GPP. In the SCOPE framework, GPP and ΦP are first simulated by the FvCB model (Farquhar et al., 1980), and then ΦF is derived based on the leaf-level empirical *ΦF-ΦP* relationship (Lee et al., 2015; van der Tol et al., 2014). Finally, SIF is computed based on the ΦF and APAR estimated from the multilayer canopy radiative transfer model within SCOPE. The goal of this section is to (1) evaluate the IAV of SIF using different ΦF-ΦP and SF parameterizations; (2) examine the IAV magnitude of modeled SIF and modeled GPP; and (3) compare the IAV of modeled instantaneous SIF at different overpass times with the daily average. The analysis including the daily average, as well as sampling at other times of day, is necessary, because it helps to evaluate theoretically how well the IAV of daily-averaged GPP and SIF can be captured from instantaneous satellite observations at different overpass times.

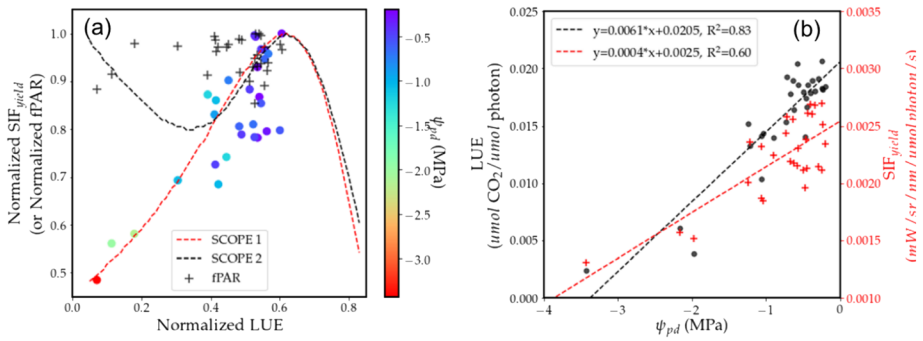

Figure 12. (a) Relative changes in *LUE* (or GPP/PAR) and SIF_{yield} (or SIF/PAR) in JJA from 2007 to 2016 overlain with modeling results of *ΦF-ΦP* relationship from the SCOPE 1 and SCOPE 2. To better compare the canopy scale observations with the modeled leaf scale, we normalize SIF_{yield} by its maximum and normalize *LUE* with the maximum at 0.6, which is the largest photochemical yield for plants exposed at normal light range. The color of the circular symbols represents ψ_{pd} (MPa), with red indicating more water stressed conditions. MODIS fPAR aggregated at 0.02° is shown and also normalized by its maximum. (b) GPP/PAR or SIF/PAR as a function of ψ_{pd}. Black and red dashed lines represent least squares linear fits to the observations.

Figure 11a shows the IAV of modeled daily average GPP and SIF with/without SF using the two different SCOPE versions. When SF is introduced as a ψ_{pd}, SIF modeled by SCOPE 1 can capture the 2012 drought to some extent, with a 17% decrease in SIF, whereas no reduction is observed for SIF modeled by SCOPE 2. This underscores the significance of choosing between two *ΦF-ΦP* options, which may lead to very different IAV patterns of SIF. When SF is fixed to 1, the IAV of SIF with both parameterizations hardly reflect the 2012 drought.

Figures 11b and 11c show the IAV of modeled GPP and SIF with different parameterizations of *ΦF-ΦP* and SF sampled at 9:30 and 13:30, respectively. During both times, SIF modeled by SCOPE 1 with SF introduced captures the 2012 drought best. A reduction of around 18% was observed at 9:30 in 2012, the magnitude of which is similar to the reduction observed for daily averages in Figure 11a, while a reduction over 25% was simulated at 13:30 since plants are usually more stressed in the afternoon due to higher VPD.

The magnitude of modeled SIF reductions (18%) in 2012 gives a theoretical reference, which we can compare against the observed SIF reductions of around 33%. We thus conclude that the large footprint of GOME-2 caused an overestimation for the forest SIF reductions because of the presence of nonforest cover within the footprints. However, the SCOPE simulations underline that we expect reductions in SIF owing to dynamic variations in plant stress, which are also comparable with the observed changes in GOME-2 SIF (about half of the reduction). It should be noted that the modeled SIF variations are always smaller than the modeled GPP variations during the 2012 drought, which is in line with our observations. A linear scaling approach for SIF-GPP would thus largely underestimate IAV in GPP, which is an important caveat for using SIF to study stress-driven IAV in GPP. In addition, our findings underline the need to better represent the stress impact on the *ΦF*, as we find that the SCOPE 2 parameterization can lead to increases in *ΦF* at low photosynthetic yields, which is unlikely to happen for plants adapted to their environment, which we will outline in the following *LUE*-SIF_{yield} section.

3.4. Smaller Variations in SIF_{yield} than LUE

Both satellite- and SCOPE-modeled SIF showed a significant decrease in the 2012 drought, but with a smaller fractional change in SIF compared to GPP. This addresses the question of the covariation between *LUE* and SIF_{yield} across different stress levels. As we observed low interannual variability in VIs during JJA, we can use this time period to better understand the connection between *LUE* and SIF_{yield} because these two terms should have a larger impact on overall GPP and SIF than changes in APAR. fPAR aggregated at 0.02° shows little variation across JJA from 2007 to 2016 (Figure 2a), indicating that the interannual GPP-SIF relationship in JJA is indeed mainly driven by SIF_{yield} changes, not APAR. Consequently, we approximated *LUE* and SIF_{yield} as GPP/PAR and SIF/PAR. In Figure 12a, we found that there is a positive correlation between *LUE* and SIF_{yield} ($R^2 = 0.66$; Figure 12a), whereas fPAR shows little variations across

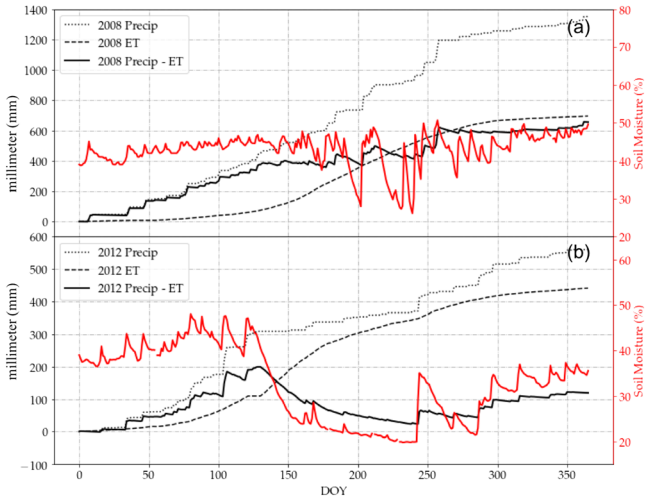

Figure 13. The water budget in (a) 2008 and (b) 2012. The black dotted line, dashed line, and solid line represent accumulated precipitation, accumulated evapotranspiration, and accumulated precipitation-accumulated evapotranspiration in the unit of millimeter (left axis). The red line represents soil moisture in the unit of percentage (right axis).

different LUE levels. Color coded by ψ_{pd}, both *LUE* and SIF_{yield} decrease in water-stressed period when ψ_{pd} is low. We also evaluated whether the SIF_{yield}-*LUE* changes observed at the canopy are consistent with leaf-level *ΦF-ΦP* employed in the SCOPE model. We found that the SCOPE 1 agrees well with our canopy measurements, with positive SIF_{yield}-*LUE* pattern and very similar changes in terms of magnitude. However, the negative SIF_{yield}-*LUE* relationship at high stress levels shown by SCOPE 2 is not observed with GOME-2. This suggests that the extreme behavior at low *ΦP* modeled in SCOPE 2 might be rarely observed in nature, as it would require stress levels that greatly exceed the capacity of NPQ for plants. Under this condition, SIF_{yield} would have to increase at higher stress levels when NPQ is saturated. This might have to do with the experimental setup, where leaf data have been used under stress conditions that go beyond what they typically experience in nature. Under these conditions, plants might lack the dissipative pathways for enhanced NPQ, which results in longer excited state lifetimes and thus higher SIF_{yields} at lower photosynthetic yields. For global modeling, the use of SCOPE 2 parametrization might thus lead to erroneous results. In the future, more studies on *ΦF-ΦP* relationships under different environmental stresses across a variety of plant species will be important to achieve more accurate estimate of SIF.

In Figure 12b, we found both *LUE* and SIF_{yield} are positively correlated with ψ_{pd} ($R^2 = 0.83$ and $R^2 = 0.60$, respectively). However, the relative change is not the same for *LUE* and SIF_{yield}. For example, when ψ_{pd} dropped from −0.5 MPa (unstressed periods) to nearly −3.5 MPa (severe drought in 2012), *LUE* dropped from 0.0175 to 0.0025—an 85% decrease—while we only see a 42% decrease from 0.00225 to 0.0013 for SIF_{yield}. This indicates that the SIF_{yield} is not as sensitive as LUE to water stress and, consequently, an ~40% fractional difference is missing with the assumption of linear SIF_{yield}-*LUE* relationship. One potential reason might be that GOME-2 SIF is measured at 9:30 a.m. when plants tend to be subjected to comparatively less stress versus the afternoon. The other reason is attributed to the systematic lower fractional reduction in SIF than GPP under the stress, which is confirmed by the SCOPE in section 3.3. Therefore, the latter one should be considered as the dominant factor explaining the smaller relative changes in the observed SIF compared to GPP. Additionally, as was previously noted, we have to bear in mind that the SIF yield changes are likely overestimated due to the large GOME-2 footprints.

4. Discussion

4.1. Seasonal Compensation of Warm Spring

A warmer spring would lengthen the photosynthetically active period and thus increase annual GPP (Buermann et al., 2013; Grippa et al., 2005; Keenan et al., 2014; Richardson et al., 2013; Sippel et al., 2017). However, we observed the opposite at the Ozarks: An early spring tends to enhance productivity and thus depletion of the soil water storage that available for the later growing season, leading to increased reliance on precipitation and higher probability of water stress and vulnerability of GPP in summer (Ummenhofer & Meehl, 2017; Wolf et al., 2016). Here we compared the water budget in 2008 (the most productive year) and 2012 (the most water stressed year) by accumulated precipitation, accumulated ET, accumulated precipitation-accumulated ET, and soil moisture in Figure 13. Compared to 2008, the ET increases much more rapidly in 2012 due to the warmer spring, leading to a significant decrease of precipitation-ET as well as soil moisture in the beginning of summer (~DOY 150), indicating that there is less water available for plants in the late growing season.

The 2008 and 2012 cases help to explain the “spring GPP gain” and “summer GPP loss” pattern shown in Figure 7, and both compensate each other in terms of annual total GPP (Figure 8d). This points to a strong coupling of the carbon and water cycles, as well as a climate-carbon feedback. Higher spring temperature with moderate VPD is accompanied with an increase in GPP and ET, which can rapidly deplete soil water

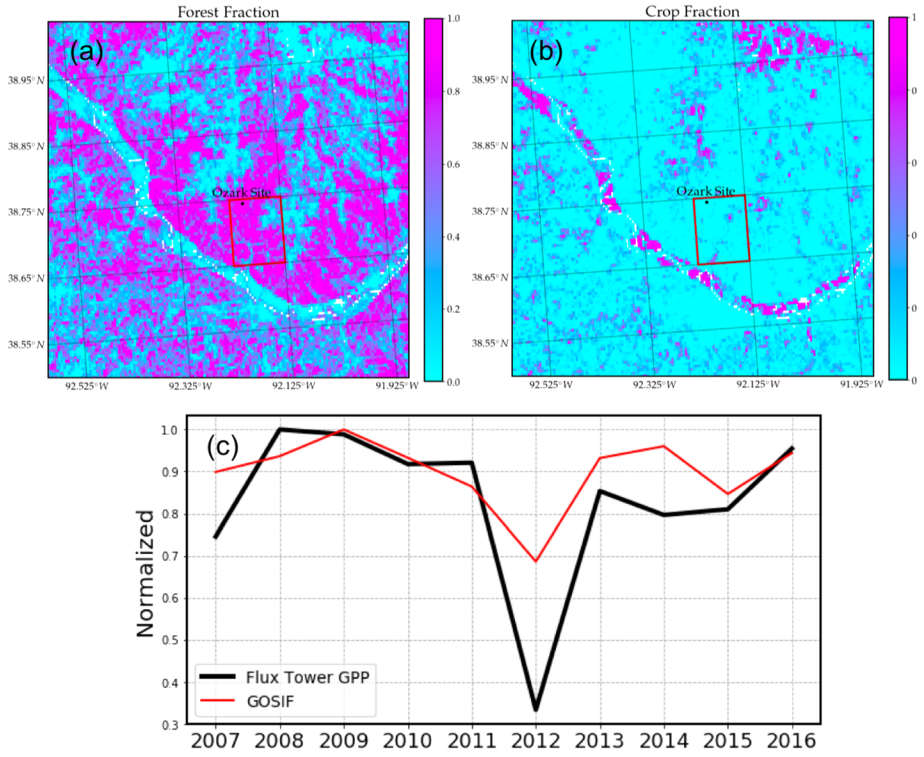

Figure 14. (a) Forest and (b) crop fraction based on the USDA CDL data set. (c) Interannual flux tower GPP, and GOSIF during JJA scaled by the corresponding maximum value from 2007 to 2016. The red boxes in (a) and (b) represent the domain for GOSIF results in (c).

available for the summer (Buermann et al., 2018; Grippa et al., 2005; Sippel et al., 2017). Therefore, during the subsequent summer, GPP is significantly reduced due to less water availability and is accompanied with a decrease in latent heat and increase in sensible heat fluxes, which ultimately leads to larger VPD and higher air temperature. This can act as a positive feedback loop, exacerbating the water and heat stress in summer. There is also a possibility that land-atmosphere coupling (Koster et al., 2006) could cause the correlation of spring-time temperature (and associated ET increases) and water deficits in summer. Although answering the question of causality of this intriguing correlation is beyond the scope of the current study, at least we found a strong correlation between spring temperature and ψ_{pd} ($R^2 = 0.52$).

With regard to changes in the seasonal cycle driven by spring-time temperature, it should be noted that the sensitivity of assimilatory and respiratory processes to spring temperature change differs by ecosystem type (Caignard et al., 2017; Wang et al., 2011; Welp et al., 2017). For example, deciduous forests are found to be more sensitive to increased spring temperature and summer drought than evergreen forests (Welp et al., 2017). More flux tower-based analyses are needed to fully understand the response of different kinds of vegetation to temperature changes. In a warming climate, there are two competing effects: increasing temperature and VPD, as well as increased water use efficiency of photosynthesis due to CO_2 fertilization (Keenan et al., 2013; Yuan et al., 2019). On the other hand, reduced transpiration due to CO_2 fertilization can also result in a positive feedback, further amplifying surface temperature increases and heat stress (Swann et al., 2016). For future projections, it will be important to understand the site-specific response and how it scales spatially. Also, process-based carbon cycle models need to better estimate the response of the ecosystem to changes in spring temperature, and the consequent energy partitioning later in the summer.

4.2. Less Reduction in SIF Than GPP in Drought Events

Both observations and SCOPE simulations show less variations in the SIF_{yield} than in *LUE* across different water stress levels (Figure 12), which explains the reduced IAV observed in SIF compared to GPP (Figures 2

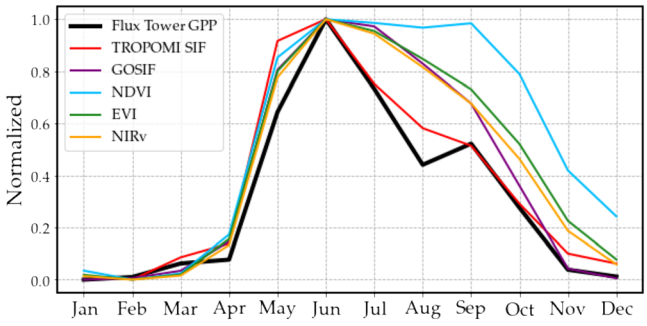

Figure 15. Monthly averaged flux tower GPP, TROPOMI SIF, GOSIF and MODIS NDVI, EVI, and NIRv in 2018. All variables are linearly normalized based on min-max scaling to fall in [0, 1].

and 11). Some recent studies suggest that SIF is more linked with chlorophyll APAR than GPP since SIF directly emanates from the light reactions of photosynthesis (Gu et al., 2019; Li et al., 2020; Porcar-Castell et al., 2014; Yang et al., 2018). In a drought period, it is expected that plants will absorb more light due to increased downwelling radiation. Meanwhile, plants are more likely to experience stomatal closure due to higher VPD and less soil water, which strongly depresses the photosynthetic efficiency. This would lead to a strong reduction in LUE while reductions in the SIF_{yield} are muted.

4.3. Promises of High-Resolution SIF Products

Current long-term SIF studies are challenged by relatively large footprints of GOME-2, especially in heterogeneous landscapes. Recently, some machine learning-based SIF products of high spatiotemporal resolution have been generated (e.g., CSIF, GOSIF, RSIF, and SIF_{oco2}) based on satellite SIF, high-resolution spectral information, and meteorology data (Gentine & Alemohammad, 2018; Li & Xiao, 2019; Turner et al., 2020; Wen et al., 2020; Yu et al., 2019; Zhang et al., 2018). In addition, TROPOMI SIF, with both high spatial and temporal resolution, has been available since early 2018 (Köhler et al., 2018). All of these data sets show promise to better understand long-term GPP:SIF relationships in different ecosystems.

We used 0.05°-monthly aggregated GOSIF and extract 2 × 2 pixels (as shown by the red boundary in Figures 14a and 14b) around the US-MOz, which cover 70% forests and 5% croplands and other landcovers (mainly grass/savannas). The choice of using 4 nearby pixels rather than the single pixel where the flux

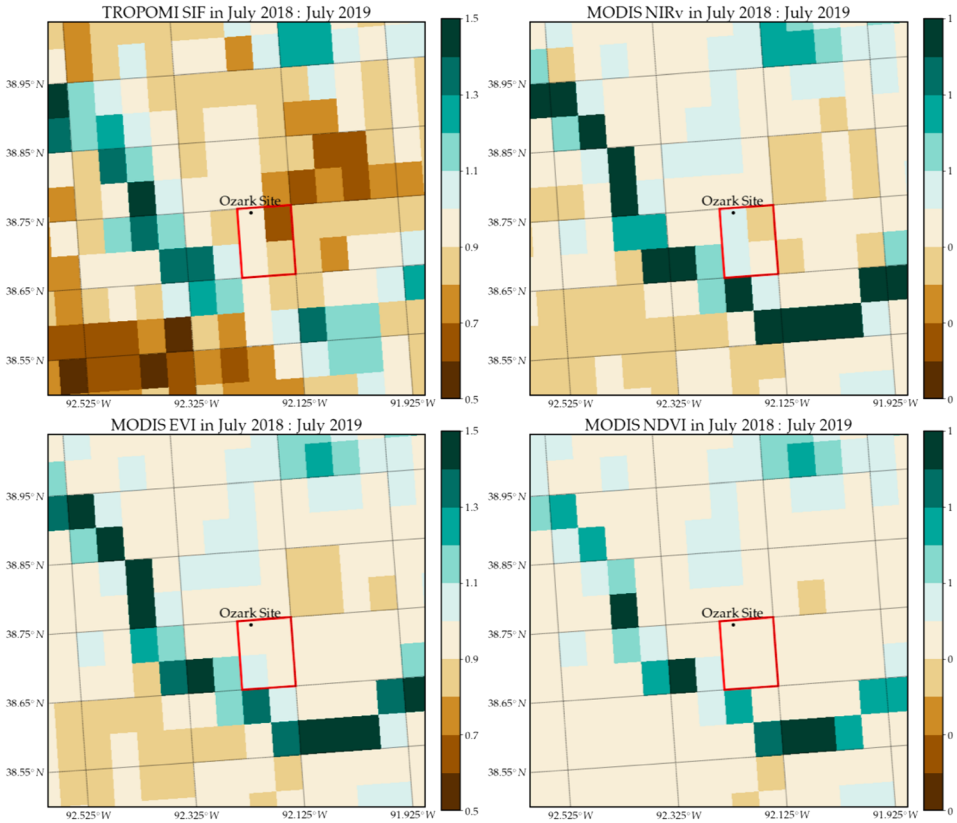

Figure 16. The spatial distributions of TROPOMI SIF, NDVI, EVI, and NIRv fractional differences in July 2018 and 2019 at 0.05° are shown in (b), (d), and (f). The full seasonal cycle for all remote sensing variables averaged over the red boundary in 2018 and 2019 is reported in Figure S4.

tower lies is that (i) uncertainties will be reduced and (ii), more importantly, the US-MOz site is dominated by southeast wind in the summer period (see https://ameriflux.lbl.gov/sites/siteinfo/US-MOz#windroses). Figure 14c shows the IAV of GOSIF versus flux tower GPP from 2007 to 2016. We observe a 30% reduction in GOSIF during the 2012 drought, which is similar to the 33% decrease in GOME-2 SIF.

We also leveraged 0.05°-monthly aggregated TROPOMI SIF in 2018 and 2019 over the same region to explore its seasonal and IAV. The Ozarks experience strong water stress in 2018 as the ψ_{pd} dropped to approximately −3.5 MPa in mid-August (Figure S3), as compared to a more normal year, 2019. Figure 15 shows the seasonality of TROPOMI SIF, GOSIF, MODIS NDVI, EVI, NIRv, and flux tower GPP in 2018. TROPOMI SIF tracks the seasonality of flux tower GPP much better than GOSIF and all MODIS VIs, with a significant decrease in July and August. As for the interannual comparison, we visualized the fractional difference of TROPOMI SIF and MODIS NDVI, EVI, and NIRv in July 2018 and 2019 (Figure 16). It shows that TROPOMI SIF over forest regions is more sensitive to water stress than all VIs, while nearby crops actually increased, either due to the proximity to rivers or watering.

5. Conclusions

At the US-MOz site, the early onset of the growing season due to a warm spring usually depletes the water storage and enhances the risk of water stress in the late growing season. As a result, spring GPP gain and summer GPP reduction compensate each other in the total annual GPP while annual net ecosystem carbon exchange is significantly reduced during warm spring years with late summer drought.

We evaluated both biophysical-based model and satellite remote sensing data to track summer GPP in the Ozarks, which usually experiences late season photosynthetic downregulation induced by water limitation. In the detailed photosynthesis modeling study using SCOPE, we found that the SF can be parameterized as a linear function of ψ_{pd}. SCOPE simulations of SIF and GPP show the ability to track interannual variations of flux tower GPP. Using remote sensing data sets, we observed that, at the seasonal timescale, GPP is largely driven by variations in absorbed radiation, which is reflected in both MODIS VIs and GOME-2 SIF. At the interannual time scale, MODIS VIs capture variations of GPP to some degree, but not as well as GOME-2 SIF. It should be noted that both the SCOPE modeling and measurements support the finding that (i) SIF contains information of both APAR and LUE and therefore has the potential to track water stress reductions in GPP and (ii) smaller variations in the SIF_{yield} (and SIF) compared to *LUE* (and GPP) are observed, with SIF anomalies muted by about a factor 3 compared to GPP if changes are purely stress driven.

However, a direct comparison between SIF and flux tower GPP is challenged by the large footprint of GOME-2 that might cover heterogeneous landscapes. Since the US-MOz site is surrounded by heterogeneous landcovers, it is challenging to attribute changes in observed SIF unequivocally to changes in absorbed light due to canopy structural changes or LUE due to physiological change. In fact, agricultural areas around the Ozark site reacted more strongly to the drought in 2012, with significant canopy structural changes, which is well captured by VIs and also affects all GOME-2 pixels. To deal with spatial heterogeneity, some recently developed machine learning-based downscaled SIF and TROPOMI SIF data sets with improved spatial and temporal resolution already show the potential to improve the monitoring of growing-season photosynthesis.

Data Availability Statement

The GOME-2 SIF product is publicly available (on ftp://fluo.gps.caltech.edu/data/Philipp/GOME-2/). The predawn leaf water potential data at the MOFLUX site are obtained online (from https://tes-sfa.ornl.gov/node/80). Flux data used in the paper are available in the AmeriFlux database (https://ameriflux.lbl.gov) before 2016, and flux data in 2016 are provided by Dr. Jeffrey D. Wood in University of Missouri, which will eventually be available through the AmeriFlux portal. All the MODIS products are obtained from Google Earth Engine (https://developers.google.com/earth-engine/datasets/catalog/modis). GOSIF data are available online (at http://globalecology.unh.edu/data/GOSIF.html). TROPOMI SIF can be downloaded online (from ftp://fluo.gps.caltech.edu/data/tropomi).

Acknowledgments

Y. Z. is supported by International Cooperation and Exchange Programs between NSFC and DFG (41761134082). J. D. W. acknowledges support for the MOFLUX site from the U.S. Department of Energy, Office of Science, Office of Biological and Environmental Research Program, through Oak Ridge National Laboratory's Terrestrial Ecosystem Science – Science Focus Area; ORNL is managed by UT-Battelle, LLC, for the U.S. DOE under Contract DE-AC05-00OR2272. Y. S. acknowledge the USDA-NIFA Hatch Project Award 1014740, the Cornell Initiative for Digital Agriculture Research Innovation Fund, the NASA Earth Science Division MEaSUREs program, and the NSF MacroSystem Biology (1926488).

References

Badgley, G., Field, C. B., & Berry, J. A. (2017). Canopy near-infrared reflectance and terrestrial photosynthesis. *Science Advances*, *3*(3), e1602244. https://doi.org/10.1126/sciadv.1602244

Beer, C., Reichstein, M., Tomelleri, E., Ciais, P., Jung, M., Carvalhais, N., et al. (2010). Terrestrial gross carbon dioxide uptake: Global distribution and covariation with climate. *Science (New York, N.Y.)*, *329*(5993), 834–838. https://doi.org/10.1126/science.1184984

Boyer, J. S., Byrne, P., Cassman, K. G., Cooper, M., Delmer, D., Greene, T., et al. (2013). The U.S. drought of 2012 in perspective: A call to action. *Global Food Security*, *2*(3), 139–143. https://doi.org/10.1016/J.GFS.2013.08.002

Buermann, W., Forkel, M., O'Sullivan, M., Sitch, S., Friedlingstein, P., Haverd, V., et al. (2018). Widespread seasonal compensation effects of spring warming on northern plant productivity. *Nature*, *562*(7725), 110–114. https://doi.org/10.1038/s41586-018-0555-7

Buermann, W., Parida Bikash, R., Martin, J., Donald Burn, H., & Reichstein, M. (2013). Earlier springs decrease peak summer productivity in North American boreal forests. *Environmental Research Letters*, *8*(2), 24027. https://doi.org/10.1088/1748-9326/8/2/024027

Buitenwerf, R., Rose, L., & Higgins, S. I. (2015). Three decades of multi-dimensional change in global leaf phenology. *Nature Climate Change*, *5*(4), 364–368. https://doi.org/10.1038/nclimate2533

Caignard, T., Kremer, A., Firmat, C., Nicolas, M., Venner, S., & Delzon, S. (2017). Increasing spring temperatures favor oak seed production in temperate areas. *Scientific Reports*, *7*(1), 8555. https://doi.org/10.1038/s41598-017-09172-7

Chen, C., Park, T., Wang, X., Piao, S., Xu, B., Chaturvedi, R. K., et al. (2019). China and India lead in greening of the world through land-use management. *Nature Sustainability*, *2*(2), 122–129. https://doi.org/10.1038/s41893-019-0220-7

Didan, K., Munoz, A. B., Solano, R., & Huete, A. (2015). "MODIS Vegetation Index User's Guide (MOD13 Series)." http://vip.arizona.edu

Dobrowski, S. Z., Pushnik, J. C., Zarco-Tejada, P. J., & Ustin, S. L. (2005). Simple reflectance indices track heat and water stress-induced changes in steady-state chlorophyll fluorescence at the canopy scale. *Remote Sensing of Environment*, *97*(3), 403–414. https://doi.org/10.1016/J.RSE.2005.05.006

Dutta, D., Schimel, D. S., Sun, Y., Tol, C. V. D., & Frankenberg, C. (2019). Optimal inverse estimation of ecosystem parameters from observations of carbon and energy fluxes. *Biogeosciences*, *16*(1), 77–103. https://doi.org/10.5194/bg-16-77-2019

Farquhar, G. D., von Caemmerer, S., & Berry, J. A. (1980). A biochemical model of photosynthetic CO_2 assimilation in leaves of C3 species. *Planta*, *149*(1), 78–90. https://doi.org/10.1007/BF00386231

Flexas, J., Escalona, J. M., Evain, S., Gulías, J., Moya, I., Osmond, C. B., & Medrano, H. (2002). Steady-state chlorophyll fluorescence (Fs) measurements as a tool to follow variations of net CO_2 assimilation and stomatal conductance during water-stress in C3 plants. *Physiologia Plantarum*, *114*(2), 231–240. http://www.ncbi.nlm.nih.gov/pubmed/11903970, https://doi.org/10.1034/j.1399-3054.2002.1140209.x

Frankenberg, C., Fisher, J. B., Worden, J., Badgley, G., Saatchi, S. S., Lee, J.-E., et al. (2011). New global observations of the terrestrial carbon cycle from GOSAT: Patterns of plant fluorescence with gross primary productivity. *Geophysical Research Letters*, *38*, L17706. https://doi.org/10.1029/2011GL048738

Frankenberg, C., O'Dell, C., Berry, J., Guanter, L., Joiner, J., Köhler, P., et al. (2014). Prospects for chlorophyll fluorescence remote sensing from the orbiting carbon Observatory-2. *Remote Sensing of Environment*, *147*(May), 1–12. https://doi.org/10.1016/J.RSE.2014.02.007

Gamon, J. A., Fred Huemmrich, K., Wong, C. Y. S., Ensminger, I., Garrity, S., Hollinger, D. Y., et al. (2016). A remotely sensed pigment index reveals photosynthetic phenology in Evergreen conifers. *Proceedings of the National Academy of Sciences of the United States of America*, *113*(46), 13,087–13,092. https://doi.org/10.1073/pnas.1606162113

Gentine, P., & Alemohammad, S. H. (2018). Reconstructed solar-induced fluorescence: A machine learning vegetation product based on MODIS surface reflectance to reproduce GOME-2 solar-induced fluorescence. *Geophysical Research Letters*, *45*, 3136–3146. https://doi.org/10.1002/2017GL076294

Grippa, M., Kergoat, L., le Toan, T., Mognard, N. M., Delbart, N., L'Hermitte, J., & Vicente-Serrano, S. M. (2005). The impact of snow depth and snowmelt on the vegetation variability over Central Siberia. *Geophysical Research Letters*, *32*, L21412. https://doi.org/10.1029/2005GL024286

Gu, L., Falge, E. M., Boden, T., Baldocchi, D. D., Black, T. A., Saleska, S. R., et al. (2005). Objective threshold determination for nighttime eddy flux filtering. *Agricultural and Forest Meteorology*, *128*(3-4), 179–197. https://doi.org/10.1016/j.agrformet.2004.11.006

Gu, L., Han, J., Wood, J. D., Christine, Y., Chang, Y., & Sun, Y. (2019). Sun-induced Chl fluorescence and its importance for biophysical modeling of photosynthesis based on light reactions. *New Phytologist*, *223*(3), 1179–1191. https://doi.org/10.1111/nph.15796

Gu, L., Massman, W. J., Leuning, R., Pallardy, S. G., Meyers, T., Hanson, P. J., et al. (2012). The fundamental equation of eddy covariance and its application in flux measurements. *Agricultural and Forest Meteorology*, *152*, 135–148. https://doi.org/10.1016/j.agrformet.2011.09.014

Gu, L., Meyers, T., Pallardy, S. G., Hanson, P. J., Yang, B., Heuer, M., et al. (2006). Direct and indirect effects of atmospheric conditions and soil moisture on surface energy partitioning revealed by a prolonged drought at a temperate forest site. *Journal of Geophysical Research*, *111*, D16102. https://doi.org/10.1029/2006JD007161

Gu, L., Pallardy, S. G., Hosman, K. P., & Sun, Y. (2016). Impacts of precipitation variability on plant species and community water stress in a temperate deciduous Forest in the central US. *Agricultural and Forest Meteorology*, *217*(February), 120–136. https://doi.org/10.1016/J.AGRFORMET.2015.11.014

Gu, L., Pallardy, S. G., Yang, B., Hosman, K. P., Mao, J., Ricciuto, D., et al. (2016). Testing a land model in ecosystem functional space via a comparison of observed and modeled ecosystem flux responses to precipitation regimes and associated stresses in a central U.S. Forest. *Journal of Geophysical Research: Biogeosciences*, *121*, 1884–1902. https://doi.org/10.1002/2015JG003302

Gu, L., Pallardy, S. G., Hosman, K. P., & Sun, Y. (2015). Drought-influenced mortality of tree species with different predawn leaf water dynamics in a decade-long study of a central US Forest. *Biogeosciences*, *12*(10), 2831–2845. https://doi.org/10.5194/bg-12-2831-2015

Guan, K., Berry, J. A., Zhang, Y., Joiner, J., Guanter, L., Badgley, G., & Lobell, D. B. (2016). Improving the monitoring of crop productivity using spaceborne solar-induced fluorescence. *Global Change Biology*, *22*(2), 716–726. https://doi.org/10.1111/gcb.13136

Guanter, L., Aben, I., Tol, P., Krijger, J. M., Hollstein, A., Köhler, P., et al. (2015). Potential of the TROPOspheric Monitoring Instrument (TROPOMI) onboard the Sentinel-5 precursor for the monitoring of terrestrial chlorophyll fluorescence. *Atmospheric Measurement Techniques*, *8*(3), 1337–1352. https://doi.org/10.5194/amt-8-1337-2015

Guanter, L., Frankenberg, C., Dudhia, A., Lewis, P. E., Gómez-Dans, J., Kuze, A., et al. (2012). Retrieval and global assessment of terrestrial chlorophyll fluorescence from GOSAT space measurements. *Remote Sensing of Environment*, *121*(June), 236–251. https://doi.org/10.1016/J.RSE.2012.02.006

Guanter, L., Zhang, Y., Jung, M., Joiner, J., Voigt, M., Berry, J. A., et al. (2014). Global and time-resolved monitoring of crop photosynthesis with chlorophyll fluorescence. *Proceedings of the National Academy of Sciences of the United States of America*, *111*(14), E1327–E1333. https://doi.org/10.1073/pnas.1320008111

He, L., Magney, T., Dutta, D., Yin, Y., Köhler, P., Grossmann, K., et al. (2020). From the ground to space: Using solar-induced chlorophyll fluorescence (SIF) to estimate crop productivity. *Geophysical Research Letters*, *47*(7), e2020GL087474. https://doi.org/10.1029/2020GL087474

Hermle, S., Lavigne, M. B., Bernier, P. Y., Bergeron, O., & Paré, D. (2010). Component respiration, ecosystem respiration and net primary production of a mature black spruce forest in northern Quebec. *Tree Physiology*, *30*(4), 527–540. https://doi.org/10.1093/treephys/tpq002

Hoerling, M., Eischeid, J., Kumar, A., Leung, R., Mariotti, A., Mo, K., et al. (2014). Causes and predictability of the 2012 Great Plains drought. *Bulletin of the American Meteorological Society*, *95*(2), 269–282. https://doi.org/10.1175/BAMS-D-13-00055.1

Huang, K., Xia, J., Wang, Y., Ahlström, A., Chen, J., Cook, R. B., et al. (2018). Enhanced peak growth of global vegetation and its key mechanisms. *Nature ecology & evolution*, *2*(12), 1897–1905. https://doi.org/10.1038/s41559-018-0714-0

Huete, A., Didan, K., Miura, T., Rodriguez, E. P., Gao, X., & Ferreira, L. G. (2002). Overview of the radiometric and biophysical performance of the MODIS vegetation indices. *Remote Sensing of Environment*, *83*(1–2), 195–213. https://doi.org/10.1016/S0034-4257(02)00096-2

Huete, A. R., Liu, H. Q., Batchily, K., & Van Leeuwen, W. (1997). A comparison of vegetation indices over a global set of TM images for EOS-MODIS. *Remote Sensing of Environment*, *59*(3), 440–451. https://doi.org/10.1016/s0034-4257(96)00112-5

Joiner, J., Guanter, L., Lindstrot, R., Voigt, M., Vasilkov, A. P., Middleton, E. M., et al. (2013). Atmospheric measurement techniques global monitoring of terrestrial chlorophyll fluorescence from moderate-spectral-resolution near-infrared satellite measurements: Methodology, simulations, and application to GOME-2. *Atmospheric Measurement Techniques*, *6*(10), 2803–2823. https://doi.org/10.5194/amt-6-2803-2013

Joiner, J., Yoshida, Y., Vasilkov, A. P., Corp, L. A., & Middleton, E. M. (2011). First observations of global and seasonal terrestrial chlorophyll fluorescence from space. *Biogeosciences*, *8*(3), 637–651. https://doi.org/10.5194/bg-8-637-2011

Karl, T. R., Gleason, B. E., Menne, M. J., McMahon, J. R., Heim, R. R. Jr., Brewer, M. J., et al. (2012). U.S. temperature and drought: Recent anomalies and trends. *Eos, Transactions American Geophysical Union*, *93*(47), 473–474. https://doi.org/10.1029/2012EO470001

Keenan, T. F., Hollinger, D. Y., Bohrer, G., Dragoni, D., Munger, J. W., Schmid, H. P., & Richardson, A. D. (2013). Increase in forest water-use efficiency as atmospheric carbon dioxide concentrations rise. *Nature*, *499*(7458), 324–327. https://doi.org/10.1038/nature12291

Keenan, T. F., Gray, J., Friedl, M. A., Toomey, M., Bohrer, G., Hollinger, D. Y., et al. (2014). Net carbon uptake has increased through warming-induced changes in temperate forest phenology. *Nature Climate Change*, *4*(7), 598–604. https://doi.org/10.1038/nclimate2253

Keenan, T. F., Migliavacca, M., Papale, D., Baldocchi, D., Reichstein, M., Torn, M., & Wutzler, T. (2019). Widespread inhibition of daytime ecosystem respiration. *Nature Ecology & Evolution*, *3*(3), 407–415. https://doi.org/10.1038/s41559-019-0809-2

Köhler, P., Guanter, L., & Joiner, J. (2015). A linear method for the retrieval of Sun-induced chlorophyll fluorescence from GOME-2 and SCIAMACHY data. *Atmospheric Measurement Techniques*, *8*(6), 2589–2608. https://doi.org/10.5194/amt-8-2589-2015

Köhler, P., Frankenberg, C., Magney, T. S., Guanter, L., Joiner, J., & Landgraf, J. (2018). Global retrievals of solar-induced chlorophyll fluorescence with TROPOMI: First results and Intersensor comparison to OCO-2. *Geophysical Research Letters*, *45*, 10,456–10,463. https://doi.org/10.1029/2018GL079031

Koster, R. D., Sud, Y. C., Guo, Z., Dirmeyer, P. A., Bonan, G., Oleson, K. W., et al. (2006). GLACE: The global land-atmosphere coupling experiment. Part I: Overview. *Journal of Hydrometeorology*, *7*(4), 590–610. https://doi.org/10.1175/JHM510.1

Lee, J.-E., Berry, J. A., van der Tol, C., Yang, X., Guanter, L., Damm, A., et al. (2015). Simulations of chlorophyll fluorescence incorporated into the Community Land Model Version 4. *Global Change Biology*, *21*(9), 3469–3477. https://doi.org/10.1111/gcb.12948

Li, Q., Chen, J., & Moorhead, D. L. (2012). Respiratory carbon losses in a managed oak forest ecosystem. *Forest Ecology and Management*, *279*, 1–10. https://doi.org/10.1016/j.foreco.2012.05.011

Li, X., & Xiao, J. (2019). A global, 0.05-degree product of solar-induced chlorophyll fluorescence derived from OCO-2, MODIS, and reanalysis data. *Remote Sensing*, *11*(5), 517. https://doi.org/10.3390/rs11050517

Li, X., Xiao, J., & He, B. (2018). Chlorophyll fluorescence observed by OCO-2 is strongly related to gross primary productivity estimated from flux towers in temperate forests. *Remote Sensing of Environment*, *204*(January), 659–671. https://doi.org/10.1016/j.rse.2017.09.034

Li, X., Xiao, J., He, B., Altaf Arain, M., Beringer, J., Desai, A. R., et al. (2018). Solar-induced chlorophyll fluorescence is strongly correlated with terrestrial photosynthesis for a wide variety of biomes: First global analysis based on OCO-2 and flux tower observations. *Global Change Biology*, *24*(9), 3990–4008. https://doi.org/10.1111/gcb.14297

Li, Z., Zhang, Q., Li, J., Yang, X., Wu, Y., Zhang, Z., et al. (2020). Solar-induced chlorophyll fluorescence and its link to canopy photosynthesis in maize from continuous ground measurements. *Remote Sensing of Environment*, *236*, 111420. https://doi.org/10.1016/j.rse.2019.111420

Lian, X., Piao, S., Li, L. Z., Li, Y., Huntingford, C., Ciais, P., et al. (2020). Summer soil drying exacerbated by earlier spring greening of northern vegetation. *Science Advances*, *6*(1), eaax0255. https://doi.org/10.1126/sciadv.aax0255

Liu, Y., Wang, J., Yao, L., Chen, X., Cai, Z., Yang, D., et al. (2018). The TanSat Mission: Preliminary global observations. *Science Bulletin*, *63*(18), 1200–1207. https://doi.org/10.1016/J.SCIB.2018.08.004

Liu, H. Q., & Huete, A. (1995). A feedback based modification of the NDVI to minimize canopy background and atmospheric noise. *IEEE Transactions on Geoscience and Remote Sensing*, *33*(2), 457–465. https://doi.org/10.1109/tgrs.1995.8746027

MacBean, N., Maignan, F., Bacour, C., Lewis, P., Peylin, P., Guanter, L., et al. (2018). Strong constraint on Modelled global carbon uptake using solar-induced chlorophyll fluorescence data. *Scientific Reports*, *8*(1), 1973. https://doi.org/10.1038/s41598-018-20024-w

Magney, T. S., Bowling, D. R., Logan, B. A., Grossmann, K., Stutz, J., Blanken, P. D., et al. (2019). Mechanistic evidence for tracking the seasonality of photosynthesis with solar-induced fluorescence. *Proceedings of the National Academy of Sciences*, *116*, 11,640–11,645. https://doi.org/10.1073/pnas.1900278116

Magney, T. S., Frankenberg, C., Fisher, J. B., Sun, Y., North, G. B., Davis, T. S., et al. (2017). Connecting active to passive fluorescence with photosynthesis: A method for evaluating remote sensing measurements of Chl fluorescence. *New Phytologist*, *215*(4), 1594–1608. https://doi.org/10.1111/nph.14662

Mallya, G., Zhao, L., Song, X. C., Niyogi, D., & Govindaraju, R. S. (2013). 2012 Midwest drought in the United States. *Journal of Hydrologic Engineering*, *18*(7), 737–745. https://doi.org/10.1061/(ASCE)HE.1943-5584.0000786

Monteith, J. L. (1972). Solar radiation and productivity in tropical ecosystems. *Journal of Applied Ecology*, *9*(3), 747–766. https://doi.org/10.2307/2401901

Myneni, Ranga, Knyazikhin, Y. & Park, T. (2015). "MCD15A3H MODIS/Terra+Aqua Leaf Area Index/FPAR 4-day L4 global 500m SIN grid V006 [data set]." NASA EOSDIS Land Processes DAAC. 2015. https://doi.org/10.5067/MODIS/MCD15A3H.006

Oleson, K., Lawrence, D. M., Bonan, G. B., Drewniak, B., Huang, M., Koven, C. D., ... Yang, Z. -L. (2013). Technical description of Version 4.5 of the Community Land Model (CLM) (No. NCAR/TN-503+STR). https://doi.org/10.5065/D6RR1W7M

Pallardy, S. G., Gu, L., Wood, J. D., Hosman, K. P., & Sun, Y. (2018). "Predawn leaf water potential of Oak-Hickory forest at Missouri Ozark (MOFLUX) site: 2004–2017." United States. https://doi.org/10.3334/CDIAC/ORNLSFA.004

Pallardy, S. G., Pereira, J. S., & Parker, W. C. (1991). Measuring the state of water stress in tree systems. In J. P. Lassoie, & T. M. Hinckley (Eds.), *Techniques and Approaches in Forest Tree Ecophysiology*, edited by (pp. 27–76). Boca Raton, FL: CRC Press.

Parazoo, N. C., Barnes, E., Worden, J., Harper, A. B., Bowman, K. B., Frankenberg, C., et al. (2015). Influence of ENSO and the NAO on terrestrial carbon uptake in the Texas-northern Mexico region. *Global Biogeochemical Cycles*, *29*, 1247–1265. https://doi.org/10.1002/2015GB005125

Park, T., Chen, C., Macias-Fauria, M., Tømmervik, H., Choi, S., Winkler, A., et al. (2019). Changes in timing of seasonal peak photosynthetic activity in northern ecosystems. *Global Change Biology*, *25*(7), 2382, gcb.14638–2395. https://doi.org/10.1111/gcb.14638

Perez-Priego, O., Guan, J., Rossini, M., Fava, F., Wutzler, T., Moreno, G., et al. (2015). Sun-induced chlorophyll fluorescence and photochemical reflectance index improve remote-sensing gross primary production estimates under varying nutrient availability in a typical Mediterranean Savanna ecosystem. *Biogeosciences*, *12*(21), 6351–6367. https://doi.org/10.5194/bg-12-6351-2015

Porcar-Castell, A., Tyystjärvi, E., Atherton, J., van der Tol, C., Flexas, J., Pfündel, E. E., et al. (2014). Linking chlorophyll a fluorescence to photosynthesis for remote sensing applications: Mechanisms and challenges. *Journal of Experimental Botany*, *65*(15), 4065–4095. https://doi.org/10.1093/jxb/eru191

Richardson, A. D., Keenan, T. F., Migliavacca, M., Ryu, Y., Sonnentag, O., & Toomey, M. (2013). Climate change, phenology, and phenological control of vegetation feedbacks to the climate system. *Agricultural and Forest Meteorology*, *169*(February), 156–173. https://doi.org/10.1016/J.AGRFORMET.2012.09.012

Rossini, M., Nedbal, L., Guanter, L., Ač, A., Alonso, L., Burkart, A., et al. (2015). Red and far red Sun-induced chlorophyll fluorescence as a measure of plant photosynthesis. *Geophysical Research Letters*, *42*, 1632–1639. https://doi.org/10.1002/2014GL062943

Running, S. W., Nemani, R. R., Heinsch, F. A., Zhao, M., Reeves, M., & Hashimoto, H. (2004). A continuous satellite-derived measure of global terrestrial primary production. *Bioscience*, *54*(6), 547–560. https://doi.org/10.1641/0006-3568(2004)054[0547:acsmog]2.0.co;2

Schimel, D., Pavlick, R., Fisher, J. B., Asner, G. P., Saatchi, S., Townsend, P., et al. (2015). Observing terrestrial ecosystems and the carbon cycle from space. *Global Change Biology*, *21*(5), 1762–1776. https://doi.org/10.1111/gcb.12822

Sippel, S., Forkel, M., Rammig, A., Thonicke, K., Flach, M., Heimann, M., et al. (2017). Contrasting and interacting changes in simulated spring and summer carbon cycle extremes in European ecosystems. *Environmental Research Letters*, *12*(7), 075006. https://doi.org/10.1088/1748-9326/aa7398

Smith, W. K., Biederman, J. A., Scott, R. L., Moore, D. J. P., He, M., Kimball, J. S., et al. (2018). Chlorophyll Fluorescence Better Captures Seasonal and Interannual Gross Primary Productivity Dynamics Across Dryland Ecosystems of Southwestern North America. *Geophysical Research Letters*, *45*, 748–757. https://doi.org/10.1002/2017gl075922

Song, L., Guanter, L., Guan, K., You, L., Huete, A., Weimin, J., & Zhang, Y. (2018). Satellite Sun-induced chlorophyll fluorescence detects early response of winter wheat to heat stress in the Indian indo-Gangetic Plains. *Global Change Biology*, *24*(9), 4023–4037. https://doi.org/10.1111/gcb.14302

Sun, Y., Frankenberg, C., Wood, J. D., Schimel, D. S., Jung, M., Guanter, L., et al. (2017). OCO-2 advances photosynthesis observation from space via solar-induced chlorophyll fluorescence. *Science*, *358*(6360), eaam5747. https://doi.org/10.1126/science.aam5747

Sun, Y., Frankenberg, C., Jung, M., Joiner, J., Guanter, L., Köhler, P., & Magney, T. (2018). Overview of solar-induced chlorophyll fluorescence (SIF) from the orbiting carbon Observatory-2: Retrieval, cross-Mission comparison, and global monitoring for GPP. *Remote Sensing of Environment*, *209*(May), 808–823. https://doi.org/10.1016/J.RSE.2018.02.016

Sun, Y., Rong, F., Dickinson, R., Joiner, J., Frankenberg, C., Lianhong, G., et al. (2015). Drought onset mechanisms revealed by satellite solar-induced chlorophyll fluorescence: Insights from two contrasting extreme events. *Journal of Geophysical Research: Biogeosciences*, *120*, 2427–2440. https://doi.org/10.1002/2015JG003150

Swann, A. L. S., Hoffman, F. M., Koven, C. D., & Randerson, J. T. (2016). Plant responses to increasing CO2 reduce estimates of climate impacts on drought severity. *Proceedings of the National Academy of Sciences of the United States of America*, *113*(36), 10,019–10,024. https://doi.org/10.1073/pnas.1604581113

Tang, J., Bolstad, P. V., Desai, A. R., Martin, J. G., Cook, B. D., Davis, K. J., & Carey, E. V. (2008). Ecosystem respiration and its components in an old-growth Forest in the Great Lakes region of the United States. *Agricultural and Forest Meteorology*, *148*(2), 171–185. https://doi.org/10.1016/j.agrformet.2007.08.008

Tucker, C. J. (1979). Red and photographic infrared linear combinations for monitoring vegetation. *Remote Sensing of Environment*, *8*(2), 127–150. https://doi.org/10.1016/0034-4257(79)90013-0

Turner, A. J., Köhler, P., Magney, T. S., Frankenberg, C., Fung, I., & Cohen, R. C. (2020). A double peak in the seasonality of California's photosynthesis as observed from space. *Biogeosciences*, *17*(2), 405–422. https://doi.org/10.5194/bg-17-405-2020

Turner, D. P., Ritts, W. D., Cohen, W. B., Gower, S. T., Running, S. W., Zhao, M., et al. (2006). Evaluation of MODIS NPP and GPP products across multiple biomes. *Remote Sensing of Environment*, *102*(3-4), 282–292. https://doi.org/10.1016/j.rse.2006.02.017

Ummenhofer, C. C., & Meehl, G. A. (2017). Extreme weather and climate events with ecological relevance: A review. *Philosophical Transactions of the Royal Society of London. Series B, Biological Sciences*, *372*(1723), 20160135. https://doi.org/10.1098/rstb.2016.0135

van der Tol, C., Berry, J. A., Campbell, P. K. E., & Rascher, U. (2014). Models of fluorescence and photosynthesis for interpreting measurements of solar-induced chlorophyll fluorescence. *Journal of Geophysical Research: Biogeosciences*, *119*, 2312–2327. https://doi.org/10.1002/2014JG002713

van der Tol, C., Verhoef, W., Timmermans, J., Verhoef, A., & Su, Z. (2009). An integrated model of soil-canopy spectral radiances, photosynthesis, fluorescence, temperature and energy balance. *Biogeosciences*, *6*. www.biogeosciences.net/6/3109/2009/

Verma, M., Schimel, D., Evans, B., Frankenberg, C., Beringer, J., Drewry, D. T., et al. (2017). Effect of environmental conditions on the relationship between solar-induced fluorescence and gross primary productivity at an OzFlux grassland site. *Journal of Geophysical Research: Biogeosciences*, *122*, 716–733. https://doi.org/10.1002/2016JG003580

Wang, X., Piao, S., Ciais, P., Li, J., Friedlingstein, P., Koven, C., & Chen, A. (2011). Spring temperature change and its implication in the change of vegetation growth in North America from 1982 to 2006. *Proceedings of the National Academy of Sciences of the United States of America*, *108*(4), 1240–1245. https://doi.org/10.1073/pnas.1014425108

Wehr, R., Munger, J. W., McManus, J. B., Nelson, D. D., Zahniser, M. S., Davidson, E. A., et al. (2016). Seasonality of temperate forest photosynthesis and daytime respiration. *Nature*, *534*(7609), 680–683. https://doi.org/10.1038/nature17966

Welp, L. R., Randerson, J. T., & Liu, H. P. (2017). The sensitivity of carbon fluxes to spring warming and summer drought depends on plant functional type in boreal forest ecosystems. *Agricultural and Forest Meteorology*, *147*(3–4), 172–185. https://doi.org/10.1016/j.agrformet.2007.07.010

Wen, J., Köhler, P., Duveiller, G., Parazoo, N. C., Magney, T. S., Hooker, G., et al. (2020). A framework for harmonizing multiple satellite instruments to generate a long-term global high spatial-resolution solar-induced chlorophyll fluorescence (SIF). *Remote Sensing of Environment*, *239*, 111644. https://doi.org/10.1016/j.rse.2020.111644

Wohlfahrt, G., & Lianhong, G. (2015). The many meanings of gross photosynthesis and their implication for photosynthesis research from leaf to globe. *Plant, Cell and Environment*, *38*(12), 2500–2507. https://doi.org/10.1111/pce.12569

Wolf, S., Keenan, T. F., Fisher, J. B., Baldocchi, D. D., Desai, A. R., Richardson, A. D., et al. (2016). Warm spring reduced carbon cycle impact of the 2012 US summer drought. *Proceedings of the National Academy of Sciences of the United States of America*, *113*(21), 5880–5885. https://doi.org/10.1073/pnas.1519620113

Wood, J. D., Griffis, T. J., Baker, J. M., Frankenberg, C., Verma, M., & Yuen, K. (2017). Multiscale analyses of solar-induced florescence and gross primary production. *Geophysical Research Letters*, *44*, 533–541. https://doi.org/10.1002/2016GL070775

Wood, J. D., Knapp, B. O., Muzika, R.-M., Stambaugh, M. C., & Gu, L. (2018). The importance of drought-pathogen interactions in driving oak mortality events in the Ozark border region. *Environmental Research Letters*, *13*(1), 015004. https://doi.org/10.1088/1748-9326/aa94fa

Yang, B., Pallardy, S. G., Meyers, T. P., Lian Hong, G., Hanson, P. J., Wullschleger, S. D., et al. (2010). Environmental controls on water use efficiency during severe drought in an Ozark Forest in Missouri, USA. *Global Change Biology*, *16*(8), 2252–2271. https://doi.org/10.1111/j.1365-2486.2009.02138.x

Yang, K., Ryu, Y., Dechant, B., Berry, J. A., Hwang, Y., Jiang, C., et al. (2018). Sun-induced chlorophyll fluorescence is more strongly related to absorbed light than to photosynthesis at half-hourly resolution in a rice paddy. *Remote Sensing of Environment*, *216*, 658–673. https://doi.org/10.1016/j.rse.2018.07.008

Yang, X., Tang, J., Mustard, J. F., Lee, J.-E., Rossini, M., Joanna, J., et al. (2015). Solar-induced chlorophyll fluorescence that correlates with canopy photosynthesis on diurnal and seasonal scales in a temperate deciduous forest. *Geophysical Research Letters*, *42*, 2977–2987. https://doi.org/10.1002/2015GL063201

Yoshida, Y., Joiner, J., Tucker, C., Berry, J., Lee, J.-E., Walker, G., et al. (2015). The 2010 Russian drought impact on satellite measurements of solar-induced chlorophyll fluorescence: Insights from modeling and comparisons with parameters derived from satellite reflectances. *Remote Sensing of Environment*, *166*(September), 163–177. https://doi.org/10.1016/J.RSE.2015.06.008

Yu, L., Wen, J., Chang, C. Y., Frankenberg, C., & Sun, Y. (2019). High-resolution global contiguous SIF of OCO-2. *Geophysical Research Letters*, *46*, 1449–1458. https://doi.org/10.1029/2018GL081109

Yuan, W., Liu, S., Zhou, G., Zhou, G., Tieszen, L. L., Baldocchi, D., et al. (2007). Deriving a light use efficiency model from eddy covariance flux data for predicting daily gross primary production across biomes. *Agricultural and Forest Meteorology*, *143*(3-4), 189–207. https://doi.org/10.1016/j.agrformet.2006.12.001

Yuan, W., Zheng, Y., Piao, S., Ciais, P., Lombardozzi, D., Wang, Y., et al. (2019). Increased atmospheric vapor pressure deficit reduces global vegetation growth. *Science Advances*, *5*(8), eaax1396. https://doi.org/10.1126/sciadv.aax1396

Zhang, Y., Joiner, J., Alemohammad, S. H., Zhou, S., & Gentine, P. (2018). A global spatially contiguous solar-induced fluorescence (CSIF) dataset using neural networks. *Biogeosciences*, *15*(19), 5779–5800. https://doi.org/10.5194/bg-15-5779-2018

Zhang, Y., Parazoo, N. C., Williams, A. P., Zhou, S., & Gentine, P. (2020). Large and projected strengthening moisture limitation on end-of-season photosynthesis. *Proceedings of the National Academy of Sciences*, *117*(17), 9216–9222. https://doi.org/10.1073/pnas.1914436117

Zhang, Y., Xiao, X., Jin, C., Dong, J., Zhou, S., Wagle, P., et al. (2016). Consistency between Sun-induced chlorophyll fluorescence and gross primary production of vegetation in North America. *Remote Sensing of Environment*, *183*, 154–169. https://doi.org/10.1016/J.RSE.2016.05.015

Zhu, Z., Piao, S., Myneni, R. B., Huang, M., Zeng, Z., Canadell, J. G., et al. (2016). Greening of the Earth and its drivers. *Nature Climate Change*, *6*(8), 791–795. https://doi.org/10.1038/nclimate3004